Journal of
Marine Science and Engineering

MDPI

Article

High-Resolution Modeling of Storm Surge Response to Typhoon Doksuri (2023) in Fujian, China: Impacts of Wind Field Fusion, Parameter Sensitivity, and Sea-Level Rise

Ziyi Xiao and Yimin Lu *

Key Laboratory of Spatial Data Mining & Information Sharing of Ministry of Education, National Engineering Research Centre of Geospatial Information Technology, Academy of Digital China (Fujian), Fuzhou University, Fuzhou 350116, China; 235520022@fzu.edu.cn
* Correspondence: luym@fzu.edu.cn; Tel.: +86-138-5015-9899

Abstract

To quantitatively assess the storm surge induced by Super Typhoon Doksuri (2023) along the complex coastline of Fujian Province, a high-resolution Finite-Volume Coastal Ocean Model (FVCOM) was developed, driven by a refined Holland–ERA5 hybrid wind field with integrated physical corrections. The hybrid approach retains the spatiotemporal coherence of the European Centre for Medium-Range Weather Forecasts (ECMWF) ERA5 reanalysis in the far field, while incorporating explicit inner-core adjustments for quadrant asymmetry, sea-surface-temperature dependency, and bounded decay after landfall. A series of numerical experiments were conducted, including paired tidal-only and full storm-forcing simulations, along with a systematic sensitivity ensemble in which bottom-friction parameters were perturbed and the anomalous (typhoon-related) wind component was scaled by factors ranging from 0.8 to 1.2. Static sea-level rise (SLR) scenarios (+0.3 m, +0.5 m, +1.0 m) were imposed to evaluate their influence on extreme water levels. Storm surge extremes were analyzed using a multi-scale coastal buffer framework, comparing two extreme extraction methods: element-mean followed by time-maximum, and node-maximum then assigned to elements. The model demonstrates high skill in reproducing astronomical tides (Pearson r = 0.979–0.993) and hourly water level series (Pearson r > 0.98) at key validation stations. Results indicate strong spatial heterogeneity in the sensitivity of surge levels to both bottom friction and wind intensity. While total peak water levels rise nearly linearly with SLR, the storm surge component itself exhibits a nonlinear response. The choice of extreme-extraction method significantly influences design values, with the node-based approach yielding peak values 0.8% to 4.5% higher than the cell-averaged method. These findings highlight the importance of using physically motivated adjustments to wind fields, extreme-value analysis across multiple coastal buffer scales, and uncertainty quantification in future SLR-informed coastal risk assessments. By integrating analytical, physics-based inner-core corrections with sensitivity experiments and multi-scale analysis, this study provides an enhanced framework for storm surge modeling suited to engineering and coastal management applications.

Keywords: storm surge; FVCOM; Typhoon Doksuri; wind field fusion; sea-level rise (SLR)

Check for updates

Academic Editor: Yannis S. Androulidakis

Received: 2 November 2025
Revised: 13 December 2025
Accepted: 15 December 2025
Published: 19 December 2025

Copyright: © 2025 by the authors. Licensee MDPI, Basel, Switzerland. This article is an open access article distributed under the terms and conditions of the Creative Commons Attribution (CC BY) license.

1. Introduction

Storm surge—an abrupt rise in local water level driven by intense meteorological disturbances such as tropical cyclones—is among the most destructive natural hazards affecting coastal regions worldwide [1]. Against the backdrop of global climate change, the combined effects of mean sea-level rise (SLR) and changes in tropical cyclone characteristics are projected to substantially elevate coastal flood risk [2,3]. Observational studies further indicate long-term changes in both the intensity of northwest Pacific tropical cyclones and the latitudinal location of their maximum intensity—including intensification of landfalling storms and poleward shifts—which together modify the hazard profile for East Asian coastlines [4,5]. Global probabilistic assessments suggest that, without effective adaptation, the frequency and severity of extreme sea-level events will increase markedly this century, amplifying exposure and vulnerability in coastal societies [6,7].

The Fujian coast of China lies within the typhoon-active northwest Pacific and features a highly convoluted shoreline, with numerous bays, estuaries, and shallow shoals. Such complex morphology, through nonlinear coupling with tides and wind stress, readily produces strong spatiotemporal heterogeneity and pronounced local amplification of storm surge response [8]. As a densely populated and economically important region, Fujian demands high-resolution surge modeling and robust risk assessment to support disaster mitigation and coastal management decisions [9].

From a numerical modeling perspective, the Finite-Volume Coastal Ocean Model (FVCOM, the University of Massachusetts Dartmouth, New Bedford, MA, USA), formulated on unstructured grids, has become a standard tool for high-resolution tide–storm surge coupling because of its geometric flexibility in representing complex shorelines and bathymetry and its strict conservation properties [10]. Nonetheless, the model's predictive skill is constrained by several key sources of uncertainty. Firstly, the accuracy of meteorological forcing is a primary limitation. Global reanalysis such as the Fifth Generation European Centre for Medium-Range Weather Forecasts (ECMWF) Atmospheric Reanalysis of the Global Climate (ERA5) provides reliable large-scale background fields but tends to systematically underestimate near-core wind speeds and gradients in the eyewall region, which can produce low bias in a simulated surge peak [11,12]. Blending a parametric typhoon model with reanalysis fields has therefore become an effective approach to retain the parametric model's near-core intensity while preserving the reanalysis-consistent far-field environment [13,14]; incorporating physical corrections such as quadrant asymmetry, sea-surface-temperature dependence, and post-landfall decay can further improve the realism of the hybrid wind field [15]. Similar hybrid strategies have been successfully applied in recent studies, such as that of Jiao et al. [16], who combined ERA5 with parametric models for Typhoon Mangkhut, and Chen et al. [17], who emphasized the role of wind stress in nonlinear surge dynamics. Similarly, Zhang, X. et al. (2024) [18] addressed ERA5's underestimation of typhoon intensity and position by reconstructing the wind field with a model incorporating a decay coefficient, successfully improving storm surge simulation accuracy for Typhoon Muifa (2022). Further refining the representation of typhoon forcing, Zhang, B. et al. (2025) [19] analyzed the joint wind-wave distributions of 35 typhoons, revealing a pronounced rightward bias in typhoon wave fields and a close correlation between wind speed and significant wave height.

Secondly, parameterizations of oceanic processes constitute another major source of uncertainty. Regional studies have shown that bottom friction parameters and wave–tide–current coupling exert significant influences on storm surge simulations, with sensitivity varying across coastal morphologies [20]. Specifically, bottom friction parameterization controls energy dissipation, and its spatial variability can markedly affect both tidal and surge simulations [21]. In shallow waters, wave-induced setup and radiation stress also contribute substantially to total water level, further underscoring the importance of accounting for wave–current coupling in detailed risk assessments [22,23].

Thirdly, interactions between sea-level rise and storm surge are inherently nonlinear; SLR not only raises the baseline water level but can modify local depths, tidal propagation, and bottom dissipation, thereby producing complex feedbacks that alter the storm surge component itself [24,25]. Moreover, the choice of extreme-value extraction method directly affects engineering and policy outcomes and therefore requires evaluation across multiple spatial scales.

Motivated by these considerations, this study develops a high-resolution FVCOM hydrodynamic model to simulate the storm surge evolution induced by Super Typhoon Doksuri (2023) along the Fujian coast and systematically assesses the effects of alternative SLR scenarios. The principal contributions of the work are as follows: (1) development of a systematically calibrated Holland–ERA5 hybrid wind field, incorporating a unified framework of physical corrections for quadrant asymmetry, sea-surface-temperature dependence, and post-landfall decay, rigorously validated against CMA best-track observations; (2) establishment and validation of a high-resolution FVCOM for astronomical tides and storm surge, followed by a systematic quantification of the spatial impacts of uncertainties in bottom friction and wind intensity on simulated surge levels; (3) comparison of two extreme-value extraction methods to assess their effect on estimated surge peaks across spatial scales; (4) analysis of storm surge response under static SLR scenarios, demonstrating its complex nonlinearity and pronounced spatial heterogeneity along the Fujian coast; and (5) provision of operationally relevant, multi-scale risk-assessment guidance for coastal engineering and emergency management.

The remainder of the paper is organized as follows. Section 2 describes the study area and data sources, details the high-resolution FVCOM configuration, and presents the Holland–ERA5 wind field blending procedure, the static sea-level-rise scenarios, and the sensitivity experiment design. Section 3 reports model validation against tidal, current, and wind observations and then presents analyses of storm surge spatiotemporal characteristics, multi-scale buffer-based exposure statistics, SLR impacts, and sensitivity results. Section 4 discusses the underlying physical mechanisms, the spatial heterogeneity of surge response, implications for engineering practice and risk management, and study limitations. Section 5 summarizes the principal conclusions and outlines priority directions for future research.

2. Materials and Methods

2.1. Study Area and Data Sources

The study domain covers the offshore waters of Fujian Province, bounded by 113–125° E and 20–31° N, and is chosen to fully encompass the track of Typhoon Doksuri (2023) and the coastal regions of Fujian potentially affected by the event. The coastline in this region is highly indented and characterized by numerous bays, estuaries, and shallow shoals. Such complex morphology, through nonlinear coupling with tides and wind stress, provides typical conditions for the generation of storm surge and for marked local amplification. To resolve shoreward shoals and estuarine-scale processes, a high-resolution nearshore grid is employed; the study area bathymetry, triangular mesh distribution, and the locations of major tide-gauge stations are illustrated in Figure 1.

Open-ocean bathymetry is based on the GEBCO_2023 grid (15″ resolution) (British Oceanographic Data Centre, Liverpool, UK) [26]. Nearshore bathymetry is replaced and refined with electronic navigational charts and regional soundings; after datum unification, these local data are merged with GEBCO to improve nearshore topographic fidelity. Coastline vectors are taken primarily from the Global Self-consistent, Hierarchical, High-resolution Geography Database (GSHHG, National Oceanic and Atmospheric Administration (NOAA), Boulder, CO, USA) [27] and subjected to manual coordinate corrections where necessary using LocaSpace Viewer 4 (Tuxingis (Suzhou) Technology Co., Ltd., Suzhou, Jiangsu, China) [28] to produce an accurate boundary for mesh generation. Using the compiled coastline and merged depth/elevation datasets, an unstructured triangular mesh was generated to balance nearshore resolution and offshore computational efficiency. Mesh resolution varies from a minimum element scale of approximately 200 m in the nearshore to a maximum of roughly 21.5 km offshore. The final mesh contains 42,333 nodes and 80,247 triangular elements. Element angles range from 30° to 120°, and adjacent element size ratios do not exceed 2.0. After mesh generation, the merged depth field was mapped to model nodes using a nearest-neighbor assignment, followed by localized smoothing and quality control to remove isolated outliers and excessively high-frequency noise, thereby reducing numerical pressure-gradient errors arising from discretized bathymetry.

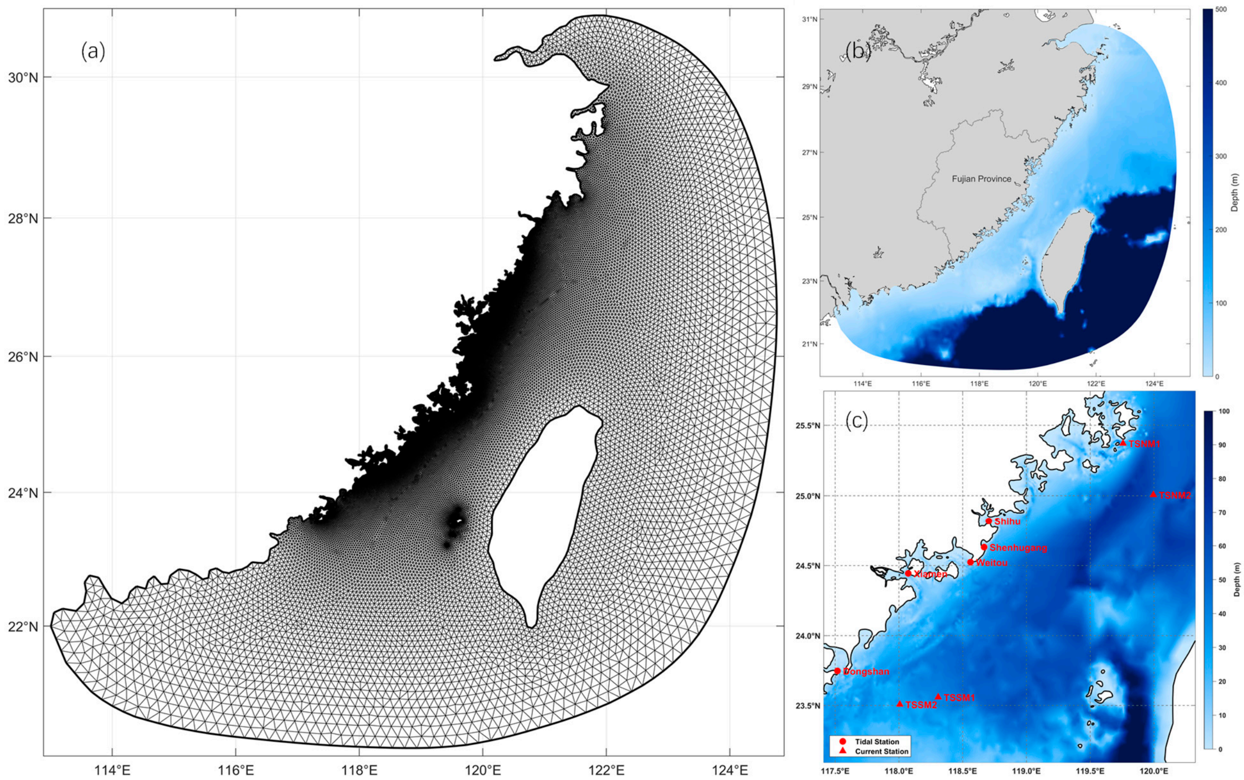

Figure 1. Composite map of the study area. (**a**) Triangular grid distribution. (**b**) Water depth distribution. (**c**) Validation station distribution.

Tidal boundary forcing is constructed from tidal harmonic constituents produced by Chinatide (developed by Ocean University of China) [29,30]. The selected constituents include major diurnal and semidiurnal and relevant overtides (e.g., K1, O1, P1, Q1, M2, S2, N2, K2, Sa, etc.). The synthesized tidal time series are temporally interpolated to the model time step and assigned to open-boundary nodes to drive interior dynamics. Where necessary, boundary time series are locally adjusted in amplitude and phase (for example, by applying linear scaling and phase shift based on nearshore tide observations) to ensure the consistency of phase and amplitude with coastal measurements; the effects of such boundary adjustments on nearshore peak timing and magnitude are assessed during post-processing. The bathymetric data from GEBCO_2023 and local charts were unified and referenced to Mean Sea Level (MSL). The tidal harmonic constituents from Chinatide were also referenced to, or adjusted to, MSL to ensure consistency in the vertical datum throughout the model domain. Thus, all model inputs and the resulting water level outputs (free surface elevation η) in this study are referenced to MSL. Overall, the data-fusion, coastline editing, mesh generation, and depth-mapping procedures described above are designed to preserve nearshore detail while minimizing numerical artifacts introduced by bathymetric discretization and boundary errors, thus providing a robust spatial foundation for FVCOM tide and storm surge simulations.

2.2. Numerical Model Configuration

Hydrodynamic simulations are performed with FVCOM v4.1 (Finite-Volume Coastal Ocean Model) [10]. FVCOM employs unstructured triangular meshes in the horizontal and a sigma (σ) coordinate in the vertical. Its finite-volume discretization ensures strict conservation and enables flexible representation of complex coastal geometry and bathymetry.

The model solves the free-surface and three-dimensional momentum equations and includes Coriolis acceleration, barotropic and baroclinic pressure gradients, horizontal and vertical turbulent viscosity, bottom friction, and surface wind stress. Vertical turbulence closure is provided by the Mellor–Yamada level 2.5 scheme [31], which is widely used for stratification and mixing processes in coastal applications. Horizontal diffusion is parameterized using a Smagorinsky formulation, with diffusion coefficients linked to shear and local grid scale.

The computational horizontal mesh, described in Section 2.1, varies from ~200 m nearshore to ~21.5 km offshore. In the vertical, the model uses 11 sigma layers. This vertical discretization follows sensitivity findings in previous storm surge studies [32] and is intended to balance computational efficiency with sufficient resolution of surface and near-bottom dynamics required to analyze bottom friction and wind stress vertical structure.

Time integration adopts a split-explicit approach that separates fast external gravity waves (barotropic mode) and slower density-driven flow (baroclinic mode). The external (barotropic) time step is set to 10 s and the internal (baroclinic) time step to 1 s. Such an explicit splitting scheme improves computational efficiency while maintaining numerical stability; implementation details follow Shchepetkin and McWilliams (2005) [33].

Bottom friction is a key control for model results, and here it is represented by a quadratic drag law. In the baseline configuration, the bottom roughness parameter z_0 is set to 8×10^{-5} m, and a minimum drag coefficient of 0.0035 is enforced to prevent nonphysical high velocities in extremely shallow elements. Given the substantial uncertainty and spatial variability in bottom friction—and its documented influence on tidal and surge dynamics in the East China Sea region [21,34]—a suite of sensitivity experiments targeting bottom-friction parameterization is described in Section 2.7 to quantify its influence on the simulated surge associated with Typhoon Doksuri.

Wetting–drying processes are activated with a threshold depth of 0.01 m to resolve tidal flat exposure and flooding dynamics in shallow coastal areas.

Open boundaries are forced by the tidal sea-level time series constructed as described above. To mitigate numerical pressure-gradient errors due to discretized bathymetry, the depth field mapped to mesh nodes is locally smoothed during model initialization.

2.3. Wind Field Construction and Physical Corrections

Accurate meteorological forcing—especially a high-fidelity typhoon wind field—is essential for realistic storm surge simulation. To overcome limitations of single data sources (for example, the ERA5 reanalysis underestimation of near-core wind speeds in tropical cyclones [35], or the lack of consistency between purely parametric models and the observed large-scale environment), this study employs a hybrid strategy that blends a parametric typhoon inner core with a reanalysis background field [14,15]. While recent studies have advanced hybrid wind field reconstruction—such as the piecewise scaling method with a distance–decay coefficient employed by Zhang, X. et al. (2024) [18] for

Typhoon Muifa, or the asymmetric Holland model combined with a large-radius linear blending used by Zhang, B. et al. (2025) [19]—the present work distinguishes itself through a more integrated and physically detailed approach. The blending is achieved with a radial weighting function to provide a smooth transition from the typhoon core to the far-field environment and is complemented by a suite of empirically validated physical corrections that enhance the wind field realism.

2.3.1. Data Sources and Preprocessing

Large-scale background wind and mean sea-level pressure fields are taken from the European Centre for Medium-Range Weather Forecasts (ECMWF) ERA5 reanalysis [11], which has a nominal horizontal resolution of ~0.25° and hourly temporal resolution, providing a reliable synoptic environment for surge forcing [36]. Typhoon Doksuri's best-track information—including center position, translation speed, central pressure, and maximum sustained wind speed—was obtained from the China Meteorological Administration (CMA) best-track dataset (https://typhoon.nmc.cn/web.html (accessed on 7 January 2025)). All meteorological fields are temporally interpolated (linear) to an hourly time series to match the model forcing cadence. The resulting fields are spatially interpolated onto the FVCOM unstructured mesh nodes and used as model surface forcing and open-boundary meteorological inputs. The generated wind field dataset spans 00:00 UTC on 21 July 2023 to 23:00 UTC on 30 July 2023, covering 240 hourly time steps (240 h) in total.

2.3.2. Parametric Typhoon Wind Field Model

For the inner-core region of the typhoon wind field, we adopt the classical axisymmetric Holland (1980) parametric model [13]. Built on the gradient wind balance, the Holland formulation provides analytic expressions for the radial distribution of sea-level pressure and gradient wind within the cyclone. The sea-level pressure $P(r)$ at radius r and the gradient wind $V_g(r)$ are expressed as

$$P(r) = P_c + (P_n - P_c)\exp\left[-\left(\frac{R_{max}}{r}\right)^B\right] \tag{1}$$

$$V_g(r) = \sqrt{\frac{B}{\rho}\left(\frac{R_{max}}{r}\right)^B (P_n - P_c)\exp\left[-\left(\frac{R_{max}}{r}\right)^B\right] + \left(\frac{rf}{2}\right)^2} - \frac{rf}{2} \tag{2}$$

where P_c is the central pressure, P_n is the environmental pressure, $R_{\max}$ is the radius of maximum wind, B is the Holland shape parameter, ρ is the air density, and f is the Coriolis parameter. The radius of maximum wind $R_{\max}$ is estimated using Graham's empirical relation [36]. The Holland shape parameter B is determined following the empirical regression of Vickery and Wadhera (2008) [37]:

$$R_{\max} = 28.52\left[0.0873(\varphi - 28) + 12.22\exp\left(\frac{P_c - 1013.2}{33.86}\right) + 0.2V + 37.2\right] \tag{3}$$

$$B = 1.881 - 0.00557 * R_{max} - 0.01295\varphi \tag{4}$$

where φ is the typhoon center latitude and V is the storm translation speed. The gradient wind computed from the Holland model is subsequently converted to the standard 10 m wind speed for use in the FVCOM wind stress calculations.

2.3.3. Hybrid Wind Field Blending Strategy

To combine the Holland model's strength in representing high wind speeds in the inner core with the ERA5 reanalysis' consistency in the large-scale environment, we employ a radial, piecewise weighted blending method [14,15]. This approach has been shown to improve typhoon wind field reconstruction in Chinese seas [15]. Two radii are defined: an inner radius, $R_{\text{inner}} = R_{\text{max}}$, and an outer radius, $R_{\text{outer}} = 3R_{\text{max}}$. The blended wind speed $V_{\text{synth}}(r)$ is given by

$$\mathrm{V}_{synth}(r) = w(r) \cdot \mathrm{V}_g(r) + [1 - w(r)] \cdot \mathrm{V}_{ERA5}(r) \quad (5)$$

with the transition weight $w(r)$ taken as a cosine smoothing function:

$$w(r) = \frac{1}{2}\left[1 + \cos\left(\pi \frac{r - R_{inner}}{R_{outer} - R_{inner}}\right)\right], R_{inner} \le r \le R_{outer} \quad (6)$$

Thus, for $r \le R_{\text{inner}}$, the blended field equals the Holland solution ($w = 1$), while for $r \ge R_{\text{outer}}$, it equals the ERA5 field ($w = 0$), and a smooth interpolation is applied in the intermediate zone. The method compensates for ERA5's tendency to underestimate near-core intensity [12,35] while preserving the spatiotemporal coherence of the far-field pressure and wind patterns.

2.3.4. Physical Corrections and Observational Calibration of the Wind Field

On top of the base hybrid field, we introduce a set of empirically based physical corrections and observational calibrations to better reproduce the observed wind structure of Typhoon Doksuri.

(1) Quadrant asymmetry correction

To represent the azimuthal asymmetry induced by storm translation and vortex dynamics, an enhancement factor Q_f is applied to the axisymmetric Holland wind field [15,38]. The modulation function emphasizes the right-forward quadrant (the dangerous semicircle) and is defined as

$$Q_f = 1.2 + 0.3 \cdot sin(\theta - \theta_m) \quad (7)$$

where θ is the azimuthal angle of a point relative to the storm center and θ_m is the storm motion direction. This correction increases eyewall wind speeds in the dangerous semicircle by approximately 20–30%, consistent with empirical observations of typhoon wind field asymmetry.

(2) Sea-surface temperature (SST) dependence

To account for thermodynamic modulation of storm intensity by ocean heat content, an SST-dependent amplification factor is introduced [4]:

$$SST_{factor} = 1 + 0.04 \cdot (SST - 27) \quad (8)$$

For an SST of 30 °C, the amplification factor equals 1.12, reflecting the stronger energy supply from the warm-pool region of the northwest Pacific.

(3) Post-landfall decay parameterization

To represent the observed decay of cyclone intensity after landfall due to increased surface friction and loss of oceanic heat flux, an empirical exponential decay is applied [39]:

$$Decay_{factor} = max\left(1 - 0.02 \cdot \left(t - t_{landfall}\right), 0.7\right) \quad (9)$$

where t_{landfall} denotes the landfall time (27 July 2023 00:00 UTC). The factor reduces wind speed by 2% per hour with a lower bound of 70% of the pre-landfall intensity. This decay is applied only over land (longitude > 118.5° E, latitude 24.5–27° N) to represent local surface effects.

(4) Observational calibration and quality control

The preliminary blended field is systematically compared against CMA best-track maximum wind observations. Polynomial fitting is used to calibrate extreme wind values during the target interval (hours 151–172) to ensure intensity consistency with observations. Quality-control procedures include a three-point weighted temporal smoother (weights 0.25–0.5–0.25) applied over hours 151–172 to remove nonphysical fluctuations, and a Gaussian moving average (9 h window) applied over hours 168–185 to suppress high-frequency noise. A per-step scaling factor is constrained to the range [0.5, 2.0] to avoid unrealistic adjustments.

Following these systematic corrections and calibrations, the synthesized wind field attains a Pearson r = 0.974 against observed maximum winds (see Section 3.1.3), indicating strong fidelity in both intensity and spatiotemporal structure and providing a high-quality meteorological forcing for the ensuing storm surge simulations.

2.3.5. Model Forcing and Uncertainty Considerations

To quantify how uncertainty in wind field intensity propagates into surge simulations, a set of sensitivity experiments was designed (see Section 2.7). Specifically, the anomalous component of the wind field during the storm's principal impact period was scaled by factors from 0.8 to 1.2 to systematically investigate the transfer function between wind-speed input errors and storm surge response, including its spatial heterogeneity (results are presented in Section 3.4). This experimental design enables the quantification of residual uncertainty in wind field construction and its effect on the final storm surge risk assessment (see Figure 2 and Table 1).

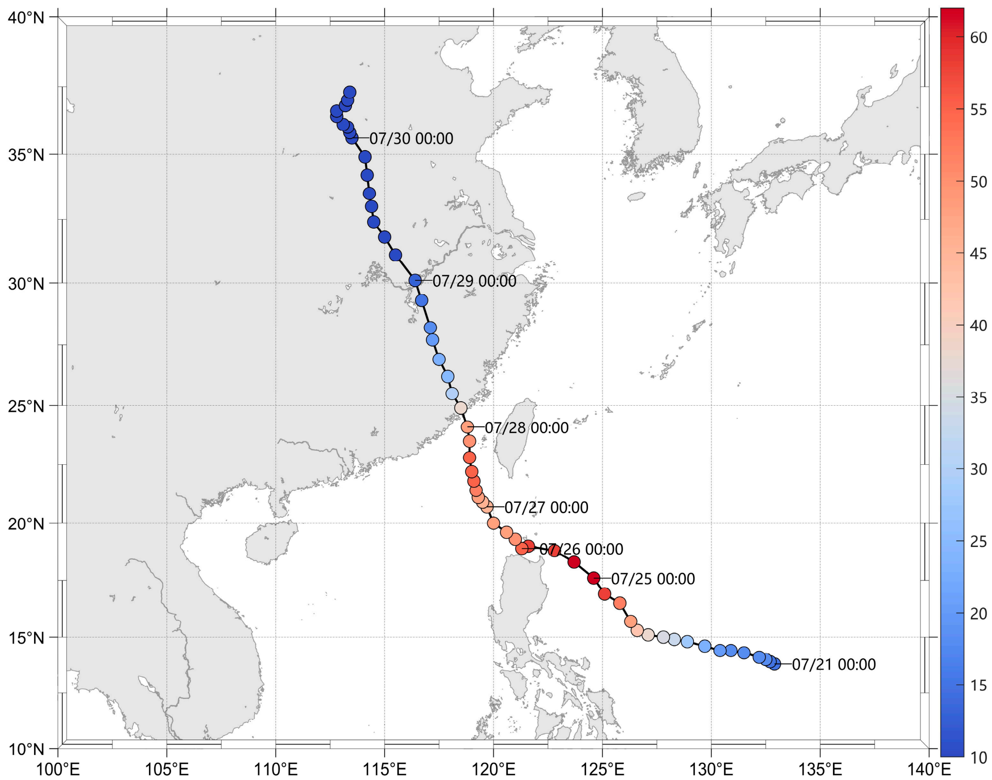

Figure 2. Typhoon track map of Doksuri (2023) (source: China Meteorological Administration Typhoon Network).

Table 1. Track information of Typhoon Doksuri (2023) (source: China Meteorological Administration Typhoon Network).

Year	Month	Day	Hour	Latitude	Longitude	Central Pressure (hPa)	Max Speed (m/s)
2023	7	25	6	18.3	123.7	915	62
2023	7	25	12	18.8	122.8	925	58
2023	7	25	18	19	121.6	925	58
2023	7	26	0	18.9	121.3	930	55
2023	7	26	6	19.3	121	940	50
2023	7	26	12	19.6	120.6	945	48
2023	7	26	18	20	120	945	48
2023	7	27	0	20.7	119.7	950	45
2023	7	27	3	20.9	119.5	950	45
2023	7	27	6	21.1	119.3	945	48
2023	7	27	9	21.4	119.2	935	52
2023	7	27	12	21.8	119.1	930	55
2023	7	27	15	22.2	119	930	55
2023	7	27	18	22.8	118.9	930	55
2023	7	27	21	23.5	118.9	940	50
2023	7	28	0	24.1	118.8	948	48
2023	7	28	3	24.9	118.5	965	38
2023	7	28	6	25.5	118.1	980	30
2023	7	28	9	26.2	117.9	990	25
2023	7	28	12	26.9	117.5	992	23
2023	7	28	15	27.7	117.2	995	20
2023	7	28	18	28.2	117.1	996	18
2023	7	28	21	29.3	116.7	996	15

2.4. Sea-Level Rise Scenarios

To assess potential future impacts of sea-level rise (SLR) on storm surge extremes and coastal inundation risk in the Fujian nearshore, three static SLR scenarios were adopted based on the authoritative conclusions of the IPCC Sixth Assessment Report (AR6) and the projection ranges from the CMIP6 multi-model ensemble: +0.3 m, +0.5 m, and +1.0 m. The scenario selection is scientifically grounded; under a medium-emission pathway (SSP2-4.5), AR6 projects global mean SLR by 2100 of approximately 0.44–0.76 m, while under a high-emission pathway (SSP5-8.5), the range is roughly 0.63–1.01 m [2]. In this study, +0.3 m represents a relatively high mid-century estimate, +0.5 m corresponds to a central 2100 estimate under a medium-emission pathway, and +1.0 m covers an extreme high-end outcome under aggressive emissions and therefore provides a conservative design margin for engineering applications. These choices are consistent with global probabilistic SLR assessments [40] and with the AR6-derived ranges cited above. This selection therefore aims to span a plausible envelope of future mean sea-level change to inform both near-term adaptation and longer-term planning.

Numerically, we adopt a static mean-surface elevation uplift to isolate the direct effect of mean SLR on surge dynamics; this control-variable approach is commonly used in surge climate assessments [41] and permits straightforward attribution of hydrodynamic changes to the prescribed elevation increment.

For clarity on numerical implementation, the static SLR scenarios are imposed relative to the Mean Sea Level (MSL) datum, which is the consistent vertical reference used for the bathymetric data (GEBCO_2023) and the tidal boundary forcing. The prescribed "static SLR" was imposed a priori in the model inputs rather than added post-processing. Concretely, the same constant ΔSLR (+0.3, +0.5, +1.0 m) was added both to the bathymetric/bed-elevation field (thereby increasing nodal water depth) and to all open-boundary tidal sea-level time series before any FVCOM runs. For each scenario, we ran (1) tidal-only simulations using the adjusted boundary time series to obtain the scenario-specific astronomical tide baseline, and then (2) full dynamical storm simulations driven by the hybrid Holland–ERA5 wind forcing using the same adjusted boundaries and initial water depths. All other model settings (vertical σ layers, wetting–drying threshold, bottom-friction parameters, time step, etc.) were held identical across scenarios to isolate the effect of the fixed elevation uplift. Because SLR was included in the dynamic model runs, the results reflect both the direct elevation shift and any nonlinear hydrodynamic consequences. All model outputs are archived at hourly resolution and processed using standardized post-processing routines for extreme-value extraction and statistical analysis, ensuring rigorous and reproducible comparisons across scenarios.

It should be noted that the static scenario approach focuses on the direct incremental effect of SLR. It does not account for potential long-term changes in tropical cyclone climate (e.g., intensity or track shifts) associated with climate change [3], nor does it explicitly include nonlinear feedback that SLR may induce via changes in local depth, tidal amplitude modulation [24], or altered surge propagation [25]. These dynamical factors are important avenues for future work and are discussed in Section 4.5. Nevertheless, the static-scenario framework provides a defensible baseline for risk assessment; its results are essential for understanding the direct consequences of SLR and for developing preliminary adaptation strategies [6]. Through this systematic experimental design, the study aims to quantify how different SLR magnitudes affect extreme total water levels and the storm surge component along the Fujian coast, thereby providing a scientific basis for regional surge risk assessment and adaptation planning.

2.5. Model Validation and Statistical Metrics

The hydrodynamic simulation period covers UTC 21 July 2023 00:00:00 to 31 July 2023 23:00:00. Observational datasets used for model validation include tide and current records from the China National Oceanographic Data Center and the China National Marine Information Center (compiled in the national Tide Tables), total water level data at Xiamen and Dongshan stations from the *China Marine Disaster Yearbook 2023*, typhoon maximum wind observations from the China Meteorological Administration (CMA) best-track reports, and surge-peak/disaster records referenced from the China Marine Information Service's 2023 marine disaster bulletin. Model performance is evaluated using the Pearson correlation coefficient r, root mean square error (RMSE), and mean bias (Bias), defined as

$$Pearson\ r = \frac{\sum_{i=1}^{n}(y_i - \overline{y})(\hat{y}_i - \overline{\hat{y}})}{\sqrt{\sum_{i=1}^{n}(y_i - \overline{y})^2 \cdot \sum_{i=1}^{n}(\hat{y}_i - \overline{\hat{y}})^2}} \tag{10}$$

$$RMSE = \sqrt{\frac{1}{N}\sum_{i=1}^{N}(y_i - \hat{y}_i)^2} \tag{11}$$

$$Bias = \frac{1}{N}\sum_{i=1}^{N}\left(\hat{y}_i - y_i\right) \tag{12}$$

where y_i denotes observations and $\hat{y}$ denotes modeled values.

2.6. Extreme-Value Extraction and Buffer Analysis

To evaluate coastal exposure systematically, we sample the coastline at regular intervals and construct along-shore normal buffers extending seaward with radii from 500 m to 5000 m. These buffers support the analysis of storm surge extremes and inundation statistics at multiple nearshore scales. Given the unstructured triangular mesh representation, two complementary element-level extreme-value extraction methods are defined and compared:

Method A (cell-averaged then time-max): At each time step, the arithmetic mean of surge at the three vertices of a triangular element is computed to yield the element's instantaneous surge, and the temporal maximum of this series is taken as the element extreme. This approach smooths node-scale variability and short-lived spikes, making it suitable for representing regional averages and mesoscale risk assessments [10,42].

Method B (node-max then assign to cell): The temporal maximum surge is first extracted at every mesh node; for each triangular element, the maximum of its three vertex node extremes is then assigned as the element extreme. Method B is more sensitive to local peaks and better captures amplification associated with narrow estuaries, shoals, and tidal channels, thus serving engineering design and operational warning applications that require fidelity to node-scale extremes.

Because this study focuses on identifying local high-risk areas for coastal engineering and inundation assessment, we adopt Method B (node-maximum then assign to cell) as the standard extreme-value extraction procedure for spatial mapping and subsequent quantitative analyses. Consequently, the storm surge spatial distributions, the Xiamen sea-level-rise spatial maps, and the sensitivity-analysis comparison maps for bottom friction and wind perturbations are all produced using Method B. For transparency, Section 3.2 presents a comparative analysis of Methods A and B.

For regional statistics and policy relevance, the Fujian coastal zone is partitioned into administrative segments (Ningde, Fuzhou, Putian, Quanzhou, Xiamen, Zhangzhou, and adjacent islands). Within each administrative segment, buffer elements are aggregated, and key indicators are reported, including element count, buffer area, area-weighted mean peak surge, and estimated inundation area. The buffer-level area-weighted mean (unit area 1 m^2) peak surge is defined as

$$\overline{\eta}_{band} = \frac{\sum_{i \in band} A_i \, \eta_i^{max}}{\sum_{i \in band} A_i} \tag{13}$$

where A_i is the element area and $\eta_i^{\max}$ is the element maximum surge (determined according to the chosen extraction method). This weighting mitigates biases introduced by heterogeneous mesh resolution and enables fairer comparisons among regions [6,43]. The spatial statistics framework is intended to provide fine-scale quantitative support for storm surge zoning and disaster-management decision-making in the Fujian coastal zone.

2.7. Sensitivity Experiment Design

To systematically assess the influence of key model parameters and meteorological forcing uncertainty on surge simulations, two sets of sensitivity experiments are designed: one targeting bottom friction parameterization and the other targeting wind field intensity.

2.7.1. Bottom-Friction Sensitivity Experiments

Bottom friction is parameterized by two independent variables: bottom roughness parameter (z_0) (unit: m) and a minimum drag coefficient ($C_{d,\min}$). Baseline values are z_0 = 8.0 × 10^{-5} m and $C_{d,\min}$ = 0.0035. Recognizing the documented spatial variability and uncertainty of bottom friction [44], each baseline parameter is perturbed by ±50%, producing z_0 = [4.0 × 10^{-5}, 8.0 × 10^{-5}, 1.2 × 10^{-4}] m and $C_{d,\min}$ = [0.00175, 0.0035, 0.00525]. These combinations yield six representative cases (case1–case6), which are compared to the baseline case (case0) (see Table 2 for details). The perturbation range is consistent with sensitivity ranges used in previous East China Sea surge studies [44,45].

Table 2. Bottom friction sensitivity experiment parameters (Case 0–Case 6: baseline and $\pm$50% perturbations of z_0 and $C_{d,\min}$).

Case	Bottom Roughness Parameter z_0(m)	Minimum Drag Coefficient $C_{d,\min}$(-)
case0	0.00008	0.0035
case1	0.00004	0.0035
case2	0.00012	0.0035
case3	0.00008	0.00175
case4	0.00008	0.00525
case5	0.00012	0.00525
case6	0.00004	0.00175

It is important to clarify that $C_{d,\min}$ represents a lower bound of the drag coefficient C_d applied in regions where vertical resolution is insufficient to resolve the bottom boundary layer (e.g., deep shelf waters), following the parameterization framework of ROMS, ECOM, and FVCOM [33,42]. The bottom roughness length z_0 is converted to C_d via the logarithmic wall law

$$C_d = \left[\frac{k}{ln\left(\frac{z_{ab}}{z_0}\right)}\right]^2 \tag{14}$$

where $k = 0.4$ is the von Kármán constant and z_{ab} is the bottom grid cell height. The actual bottom friction stress is calculated nonlinearly as $\tau = \rho C_d \mid u \mid u$ (ρ: seawater density; u: current speed), so a 50% change in $C_{d,\min}$ (e.g., 0.0035→0.00525) does not imply linear variation in τ (typically inducing ~30% stress change for moderate currents).

For each parameter combination, we perform two types of simulations: tidal-only runs and full storm-forcing surge runs. This design isolates the distinct responses of tidal dynamics and wind-driven surge to bottom-friction parameter changes [10], thereby characterizing the relative role of friction in modulating tide propagation and surge energy dissipation.

2.7.2. Wind Intensity Sensitivity Experiments

Given ERA5's documented tendency to underestimate near-core wind intensity [12] and the intrinsic uncertainty in hybrid wind field construction, a controlled experiment suite is implemented to assess how wind intensity errors propagate to surge response. Starting from the baseline blended wind field, the anomalous wind component during the storm's main impact period is identified and scaled by 0.8, 0.9, 1.1, and 1.2 to generate four wind scenarios (Case1–Case4). This procedure alters only wind magnitude while preserving spatial structure and temporal phasing, thereby isolating the effect of wind-speed changes on surge response [41].

The linear scaling of wind speed perturbs the surface wind stress nonlinearly [46], which is expected to produce a non-proportional surge response. In these wind-sensitivity experiments (Case1–Case4), the bottom-friction parameters and all other physical parameterizations are maintained identical to the baseline case. This experimental design isolates the effect of wind intensity variations.

Consequently, all simulations in this suite utilize the same FVCOM configuration detailed in Section 2.2, encompassing the computational mesh, vertical layering, time stepping, and turbulence closure scheme. Any differences in the model outputs—which include hourly time series of total water level, astronomical tide, and derived storm surge—can therefore be attributed unequivocally to the prescribed changes in wind intensity. These outputs form a consistent basis for the quantitative analyses in Section 3.4 and the mechanistic discussions in Section 4.3.

3. Results

3.1. Model Validation

3.1.1. Tide (Astronomical Tide) Validation

Figure 3 and Table 3 present time-series comparisons and statistical metrics for simulated and predicted astronomical tide from the national Tide Tables at five tide stations: Shihu, Shenhugang, Weitou, Xiamen, and Dongshan. The model captures the amplitude and phase of the principal tidal signals at all stations, with correlation coefficients (Pearson r) exceeding 0.97 (Shihu 0.979, Shenhugang 0.986, Weitou 0.985, Xiamen 0.992, Dongshan 0.993). For example, at Shihu, the national Tide Tables peak tide was 1.58 m at 20:00 UTC on 25 July 2023, whereas the simulated peak was 1.51 m, giving an absolute error of 0.07 m and identical peak timing. The scatter plot (Figure 4) further shows that simulated values cluster tightly about the 1:1 line, the regression slope is close to unity, and no substantial systematic bias is apparent.

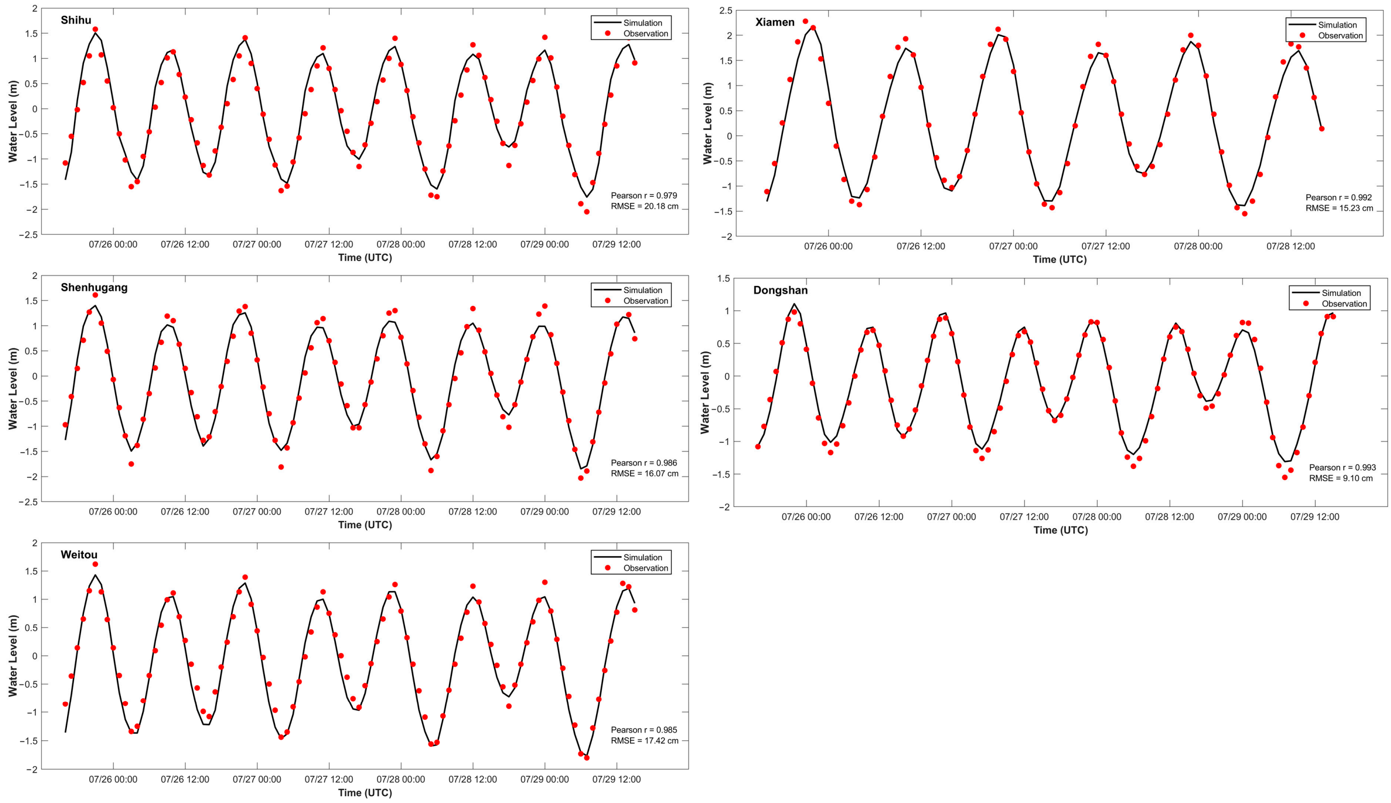

Figure 3. Observed vs. modeled tidal time series at five tide stations (UTC 25 July 2023 16:00–29 July 2023 15:00). Vertical datum: water levels are referenced to the long-term Mean Sea Level (MSL).

Table 3. Tide water level validation statistics for five tide stations.

Station/Tide Water Level	Number of Samples	Longitude	Latitude	Pearson r	Bias (m)	RMSE (m)
Shihu	96	118.7	24.8167	0.9789	0.0544	0.2018
Shenhugang	96	118.6667	24.6333	0.9858	−0.0041	0.1607
Weitou	96	118.5667	24.5167	0.9854	−0.058	0.1742
Xiamen	73	118.0667	24.45	0.9922	−0.0285	0.1523
Dongshan	96	117.5167	23.75	0.9933	0.0305	0.091

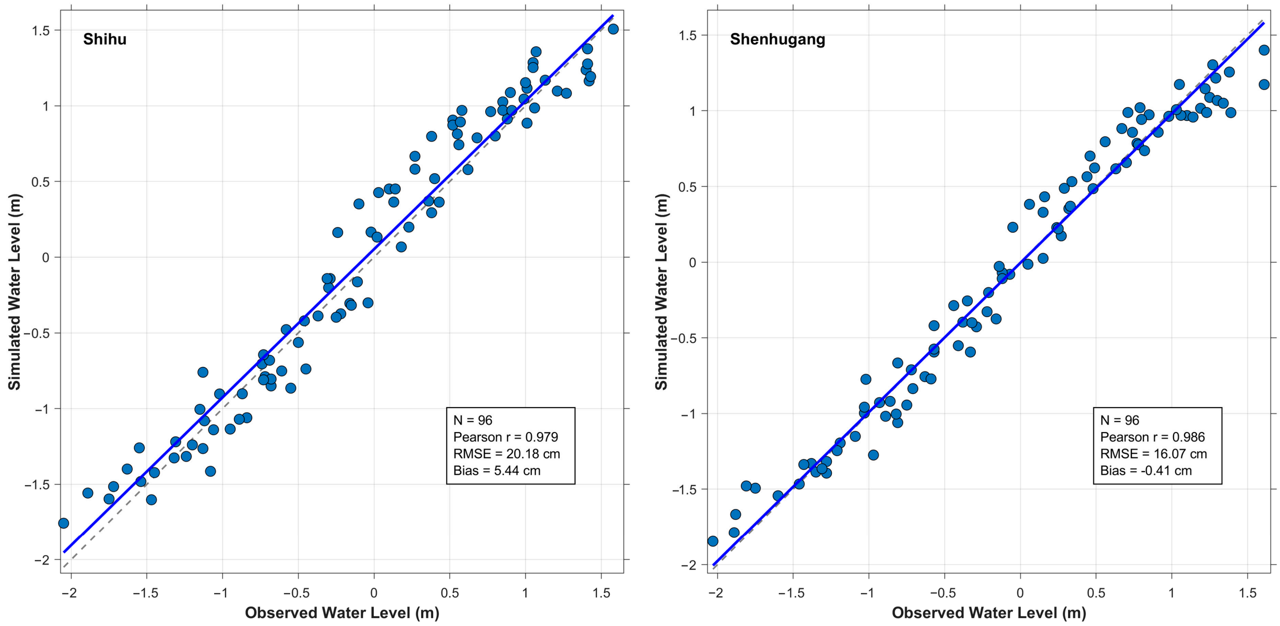

Figure 4. Scatter plot of observed vs. simulated tide water levels with regression statistics. Vertical datum: water levels are referenced to the long-term Mean Sea Level (MSL).

The root mean square errors (RMSE) range from approximately 0.09 to 0.20 m across the stations (Table 3). The discrepancies here (up to ~0.2 m during extreme high water) are not uncommon for high-resolution, coupled tide–storm surge simulations along topographically complex coastlines like Fujian, and can arise from multiple sources: phase and amplitude errors in open-boundary tidal forcing, uncertainties introduced by nearshore bathymetric and coastline simplification, and spatially nonuniform effects of bottom-friction parameterization on tide propagation and dissipation [10,21,44]. In addition, nonlinear tide–wave interactions under strong wind forcing and far-field wave propagation can modulate high-water residuals [22,23]. Further analysis and targeted numerical experiments addressing these error sources are presented in Sections 3.4 and 4.3.

3.1.2. Current (Speed/Direction) Validation

Figure 5 shows time-series comparisons of observed and simulated current speed and direction at four tidal-current stations located at the northern and southern entrances of the Taiwan Strait. As summarized in Table 4, the model captures the periodic variability and peak characteristics of current speed reasonably well; Pearson r for speed ranges from 0.79 to 0.93 and RMSE values lie between 0.096 and 0.140 m/s, indicating that the modeled hydrodynamic background is adequate to support storm surge simulation [10].

Discrepancies appear in current direction, with direction RMSEs between 33.6° and 52.6°, and the deviations are most pronounced during rapid direction changes or high-speed phases. Directional errors of this magnitude are not uncommon in coastal models for complex bathymetry [47]; the physical mechanisms and implications for the present study's objectives are discussed in Section 4 in conjunction with sensitivity experiment results. Given that this study focuses on surge maxima driven principally by wind stress and pressure gradients, and since the model reproduces astronomical tides and surge time series satisfactorily (Sections 3.1.1 and 3.1.3), the documented direction errors are not expected to materially affect conclusions regarding surge peak water levels.

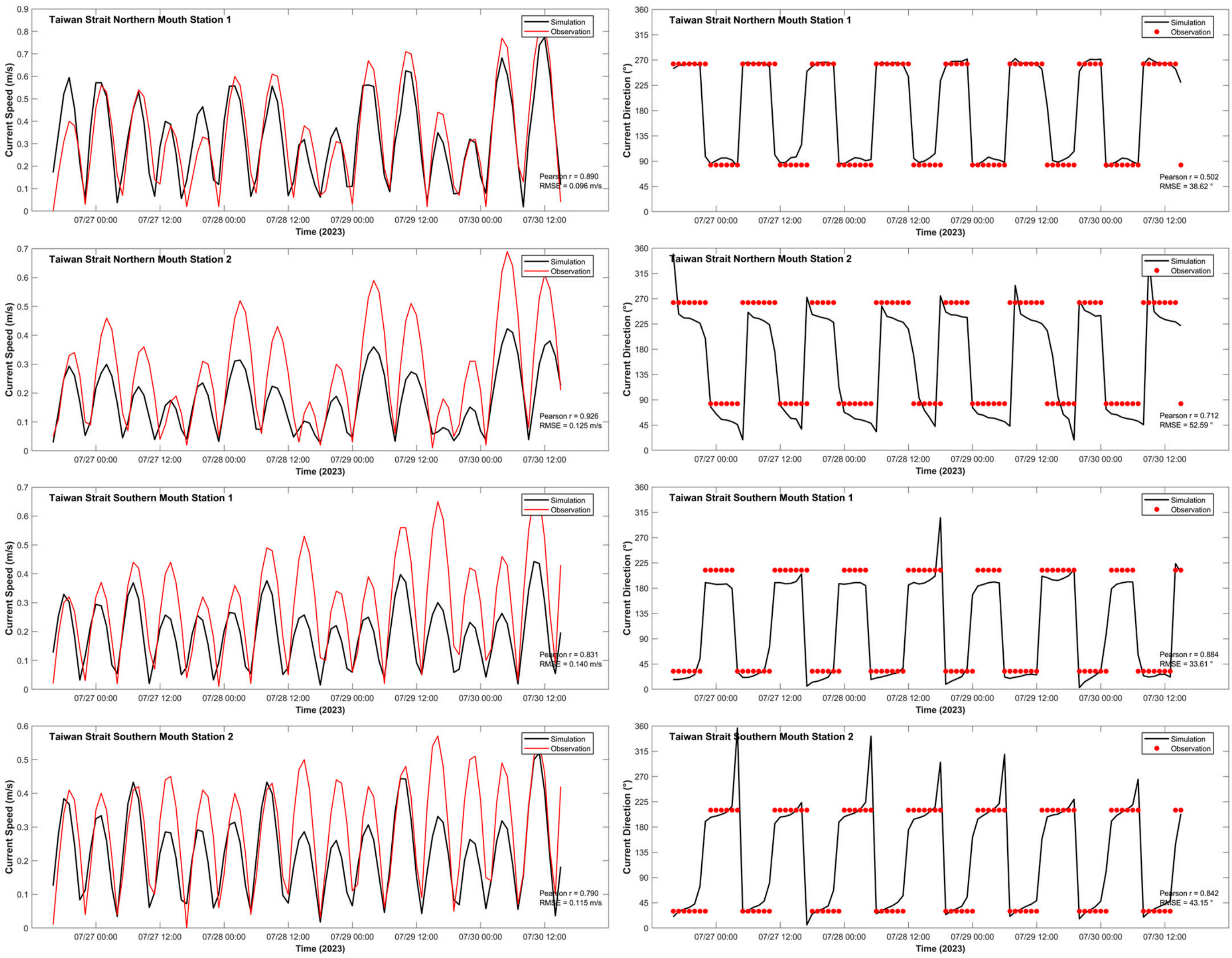

Figure 5. Time series comparison of observed vs. simulated current velocity and direction at four current stations.

Table 4. Statistical metrics for observed vs. simulated current velocity and direction at four current stations.

Station/Speed	**Number of Samples**	**Longitude**	**Latitude**	**Pearson r**	**Bias (m/s)**	**RMSE (m/s)**
TSNM 1	96	119.755	25.37	0.8896	−0.013	0.0957
TSNM 2	96	120	25	0.926	−0.093	0.1248
TSSM 1	96	118.3333	23.5283	0.8306	−0.1012	0.1401
TSSM 2	96	118	23.5	0.7897	−0.071	0.1151
Station/Direction	Number of samples	Longitude	Latitude	Pearson r	Bias (°)	RMSE (°)
TSNM 1	96	119.755	25.37	0.5024	6.44	38.62
TSNM 2	96	120	25	0.7123	−13.3	52.59
TSSM 1	96	118.3333	23.5283	0.8843	−5.93	33.61
TSSM 2	96	118	23.5	0.8423	12.82	43.15

3.1.3. Forcing Wind Field Validation

This subsection evaluates the Holland–ERA5 hybrid wind field constructed in Section 2.3 against near-surface observations for Typhoon Doksuri. As shown in Figure 6, maximum wind speeds derived from the hybrid field match CMA best-track observations closely, yielding a Pearson r = 0.974. This represents a substantial improvement over the direct use of ERA5 reanalysis which systematically underestimates near-core wind intensity [12,35].

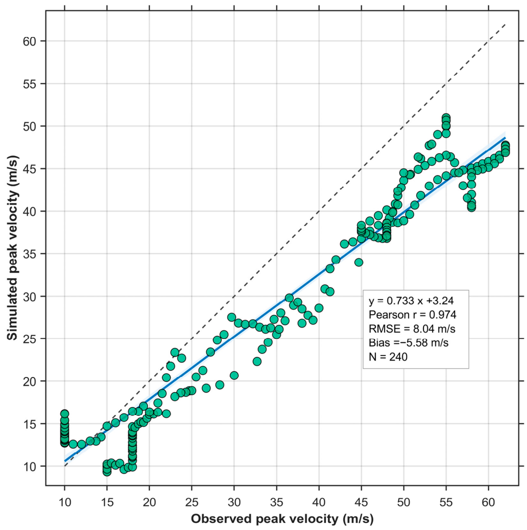

Figure 6. Scatter plot of observed maximum wind speed (CMA typhoon reports) vs. modeled Holland + ERA5 maximum wind speed.

To illustrate spatial improvements, Figures 7 and 8 present comparative sequences of the original ERA5 and the hybrid wind fields at 6 h intervals from 18:00 UTC 26 July to 00:00 UTC 28 July 2023. The hybrid field exhibits a more compact wind-speed gradient and stronger extrema near the typhoon center, more faithfully representing the inner-core pressure–wind structure. Such structural improvements are crucial for accurately representing the primary drivers of storm surge—wind stress and pressure gradients—and their hydrodynamic effects are examined further in the wind field sensitivity analysis (Section 3.4).

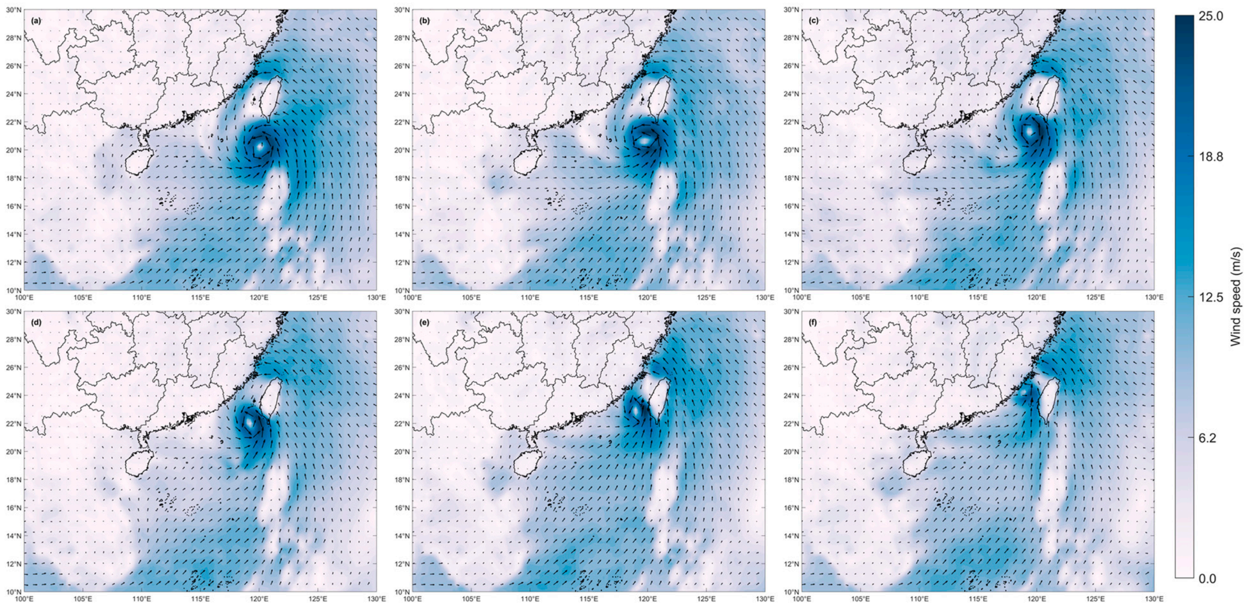

Figure 7. ERA5 reanalysis wind speed fields (26 July 2023 18:00–28 July 2023 00:00 UTC, six-hourly intervals; subplots (**a**–**f**)).

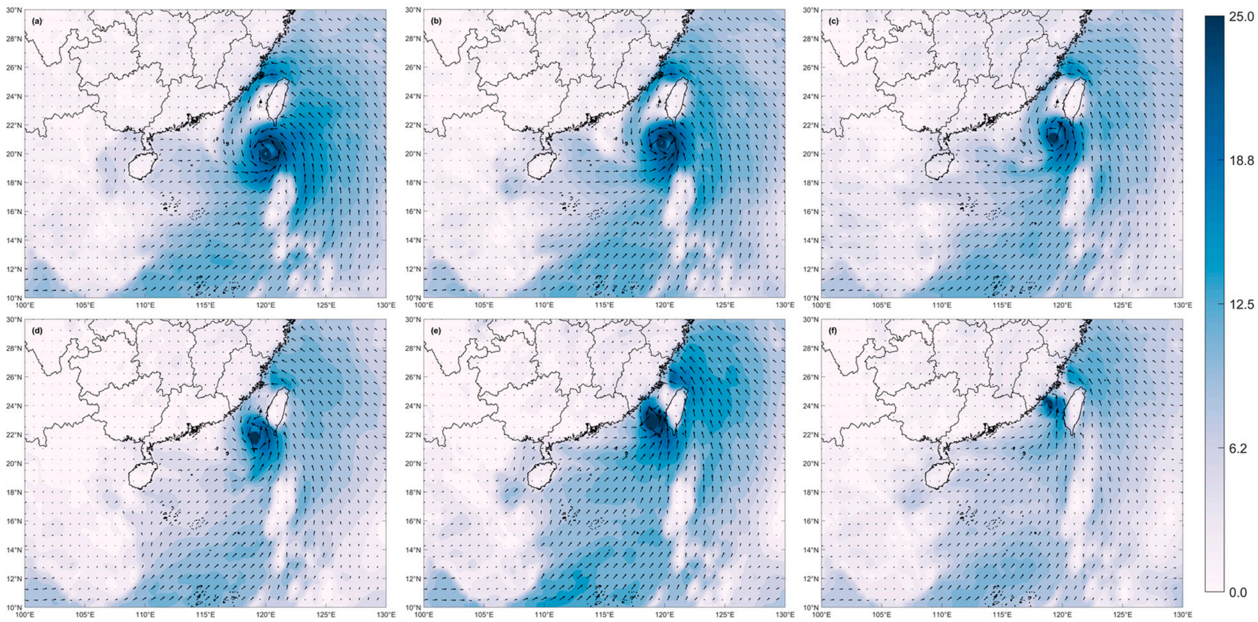

Figure 8. Holland + ERA5 hybrid wind speed fields (26 July 2023 18:00–28 July 2023 00:00 UTC, six-hourly intervals; subplots (**a**–**f**)).

3.1.4. Water-Level Validation

Driven by the validated Holland–ERA5 hybrid wind field, the FVCOM was used to simulate the full storm surge evolution of Typhoon Doksuri.

Figure 9 shows time-series comparisons of observed and simulated total water level (astronomical tide + surge) at two representative tide stations, Xiamen and Dongshan. The agreement with observations is strong; Xiamen achieves Pearson r = 0.987 and RMSE = 0.198 m and Dongshan achieves Pearson r = 0.985 and RMSE = 0.136 m. The model captures both the water level peak magnitudes and their temporal evolution, indicating that the high-resolution mesh, physical parameterizations, and hybrid wind forcing collectively provide a reliable representation of surge dynamics.

Taken together, the validation results in Sections 3.1.1–3.1.4 indicate robust model performance for astronomical tide, hybrid wind forcing, and water levels. Although localized deviations of ~0.1–0.2 m and directional errors exist, the overall accuracy satisfies the requirements of subsequent extreme-value analyses and SLR-impact assessments.

3.2. Spatiotemporal Characteristics of Storm Surge and Coastal Exposure Analysis

Figure 10 displays an hourly water level and storm surge time series for major tide stations during Typhoon Doksuri. Simulated surge and water level peaks at most coastal stations concentrate between 22:00 and 23:00 UTC on 27 July 2023, reflecting the co-control of typhoon track, distribution of maximum winds and tidal phase on peak timing. Spatially (Figure 11), surge is markedly amplified in the nearshore zone, with pronounced local enhancement in recessed coastlines, estuaries and shoal areas. These nearshore amplification effects can be explained by geometric confinement and energy-convergence mechanisms in shallow areas; shoals and estuaries concentrate tidal- and wind-driven flow, thereby amplifying sea-level response [24,32]. The distribution of maximum total water level (Figure 12) further shows substantially higher maxima near the shore relative to offshore, with the localized maximum water level approaching ~2.8 m—typical of terrain–tide–wind coupling amplification and consistent with regional and global analyses [48].

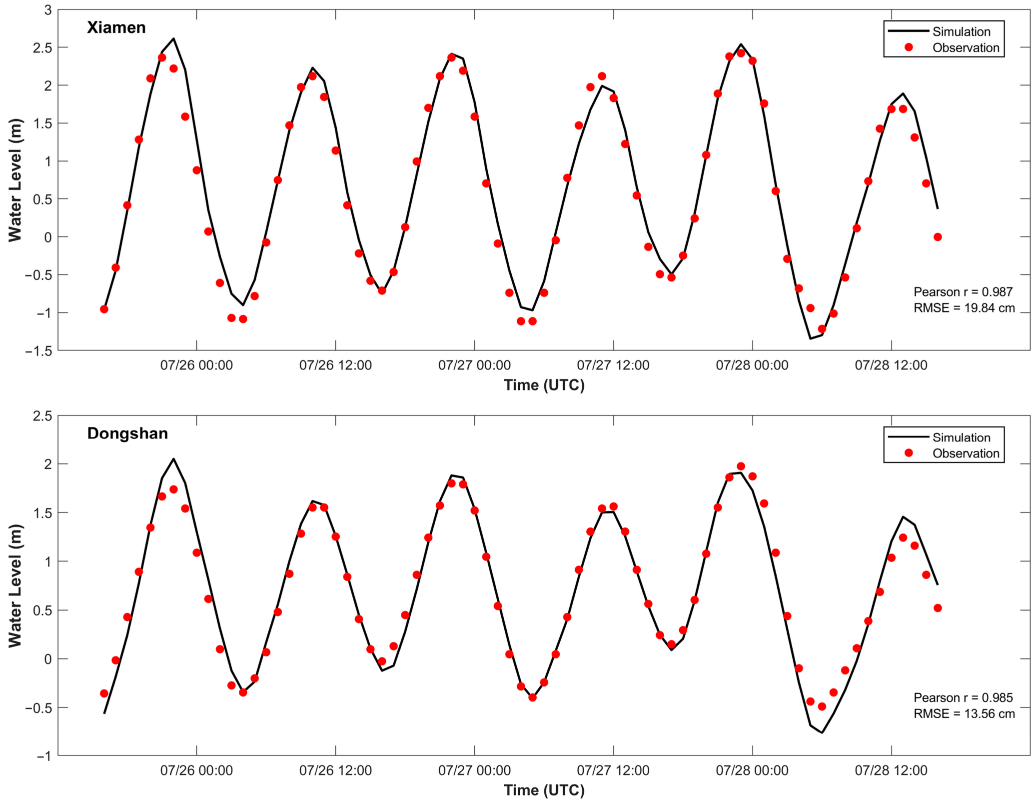

Figure 9. Time series comparison of observed vs. simulated water levels at Xiamen and Dongshan stations. Vertical datum: water levels are referenced to the long-term Mean Sea Level (MSL).

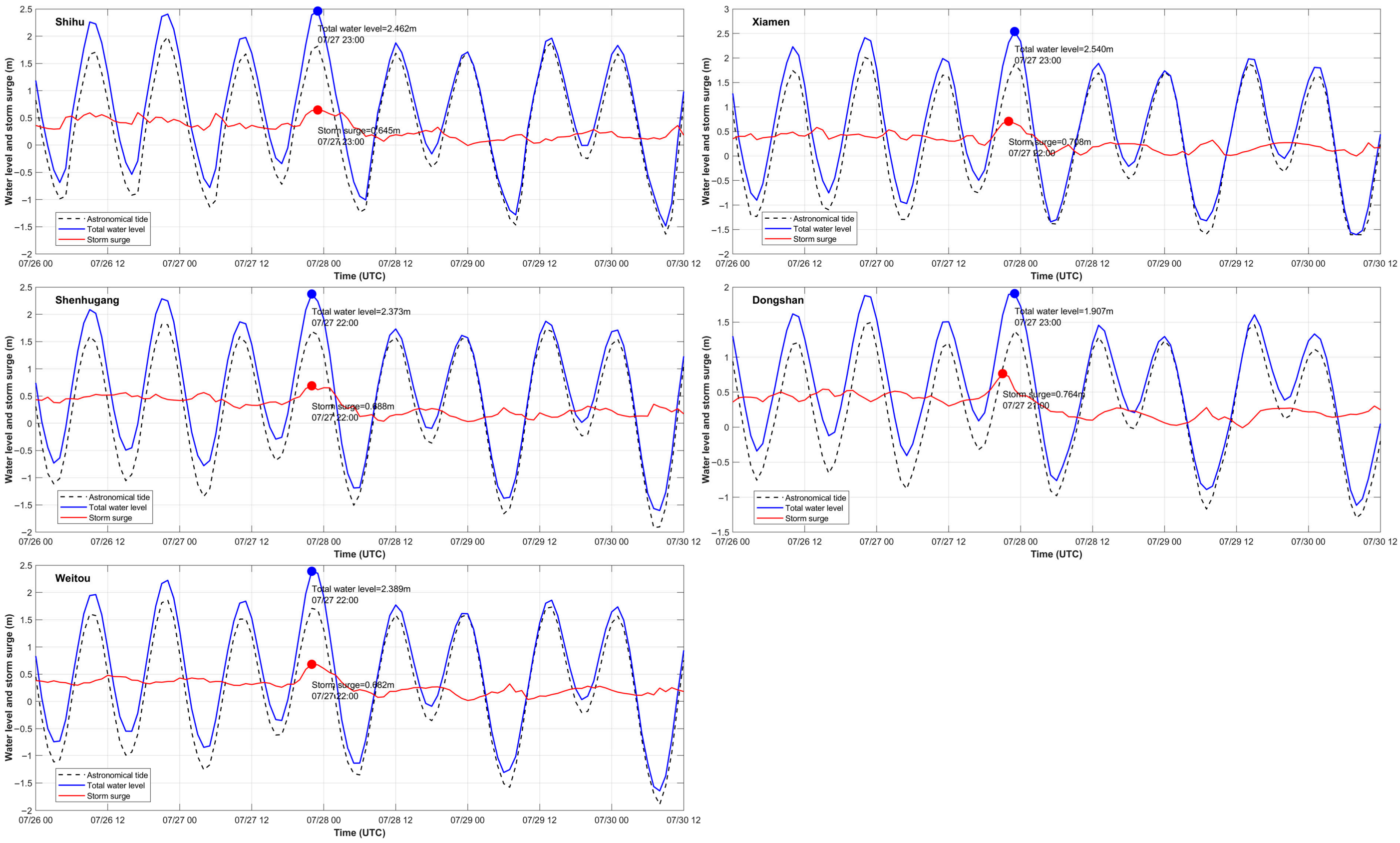

Figure 10. Time series of astronomical tide, total water level, and storm surge at Shihu, Shenhugang, Weitou, Xiamen, and Dongshan Stations (UTC 26 July 2023 to 30 July 2023).

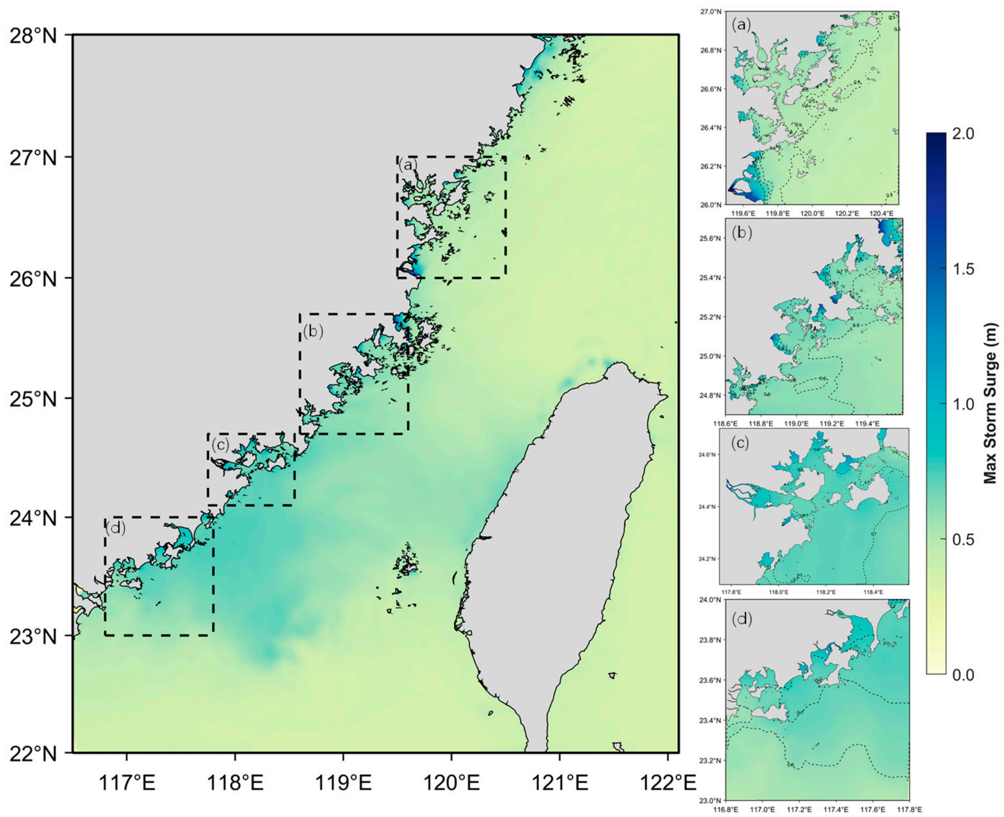

Figure 11. Spatial distribution of maximum storm surge during Typhoon Doksuri; unit: m. (**a**–**d**) are close-up views of specific nearshore areas corresponding to the marked regions in the main panel.

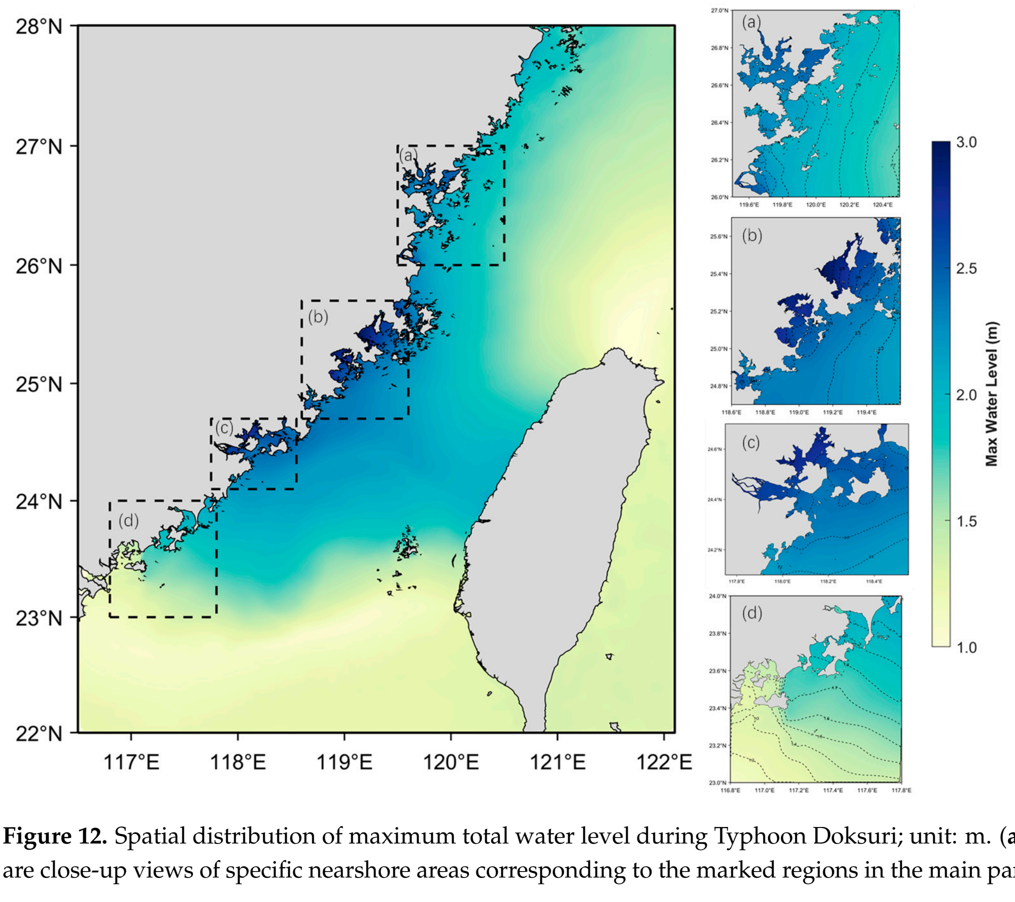

Figure 12. Spatial distribution of maximum total water level during Typhoon Doksuri; unit: m. (**a**–**d**) are close-up views of specific nearshore areas corresponding to the marked regions in the main panel.

To systematically assess the sensitivity of coastal exposure to statistical scale and extreme-value extraction method, buffers with radii from 500 m to 5000 m were constructed normal to the coastline (Figure 13, left). Two reduction methods were compared: Method A (cell-averaged then time-max) and Method B (node-max then assign to cell). City-grouped statistics based on Method B are presented in Figure 13 (right), and detailed values are given in Appendix A, Table A1. Comparing these extraction procedures highlights the inherent trade-off between representing local extreme values and achieving stable spatial statistics, which is a crucial aspect of scale-dependent risk assessment.

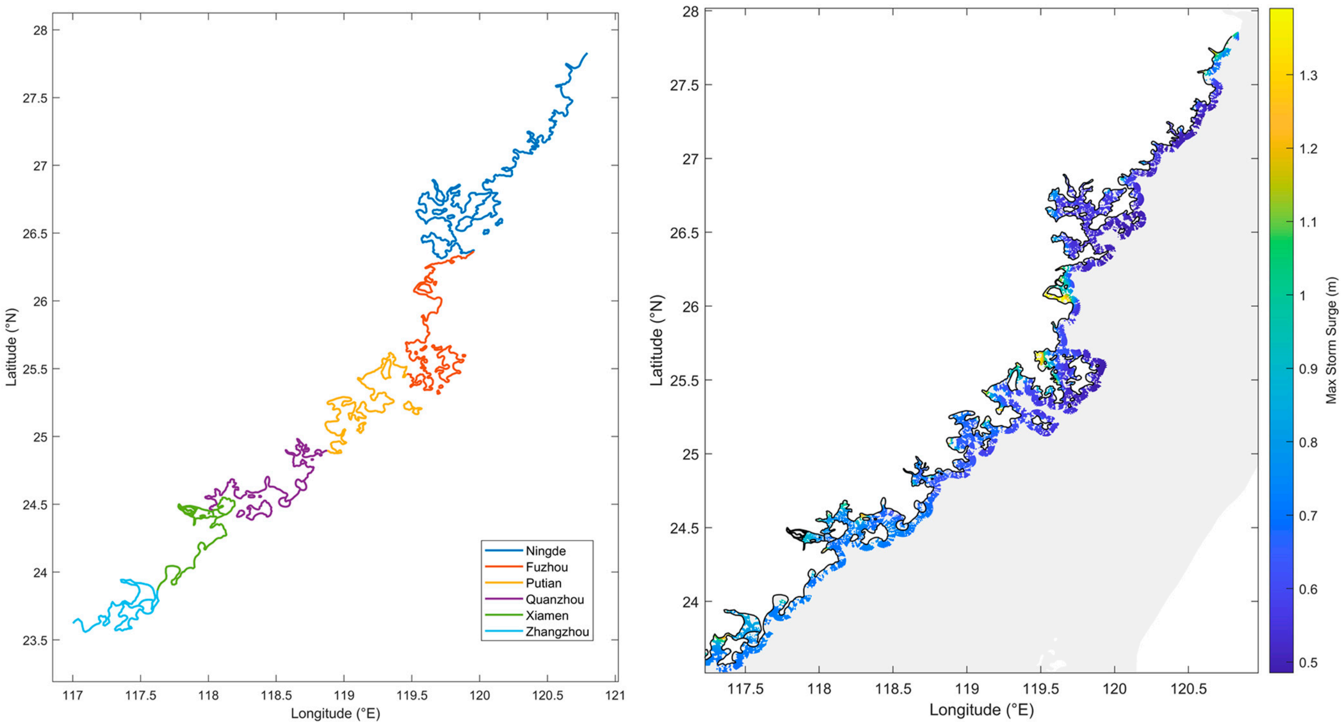

Figure 13. Composite map for buffer analysis. Left: Coastline map divided by administrative divisions (Ningde, Fuzhou, Putian, Quanzhou, Xiamen, Zhangzhou, and adjacent islands). Right: Maximum storm surge extraction via Method B at 5000 m buffer distance.

Statistics show that the node-based extraction (Method B) systematically yields larger area-normalized maximum surge values than the cell-averaged extraction (Method A) for all cities and buffer scales (Appendix A, Table A1). Absolute differences (Δ = mean_B − mean_A) range from 0.006 to 0.034 m, corresponding to relative differences of ≈0.8–4.5%. These positive Δ values indicate the methodological sensitivity of the reduction procedure—Method B preserves node-scale extremes (and thus captures local spikes in narrow estuaries, shoals and channels), while Method A's element-level averaging suppresses such spikes and better represents regional means.

Area-weighted maximum storm surge: As buffer width increases from 500 m to 5000 m the area-weighted maximum surge generally declines across most cities (Figure 14), indicating that surge magnitudes are concentrated in the immediate nearshore and are progressively diluted when larger offshore areas—whose surge values are systematically lower—are included. For example, Fuzhou's area-weighted peak falls substantially when the buffer is expanded to 5 km (from 0.7814 m (500 m) to 0.6676 m (5000 m), a reduction of 0.1138 m (≈14.6%), see Appendix A, Table A1), illustrating the strong nearshore concentration of surge response.

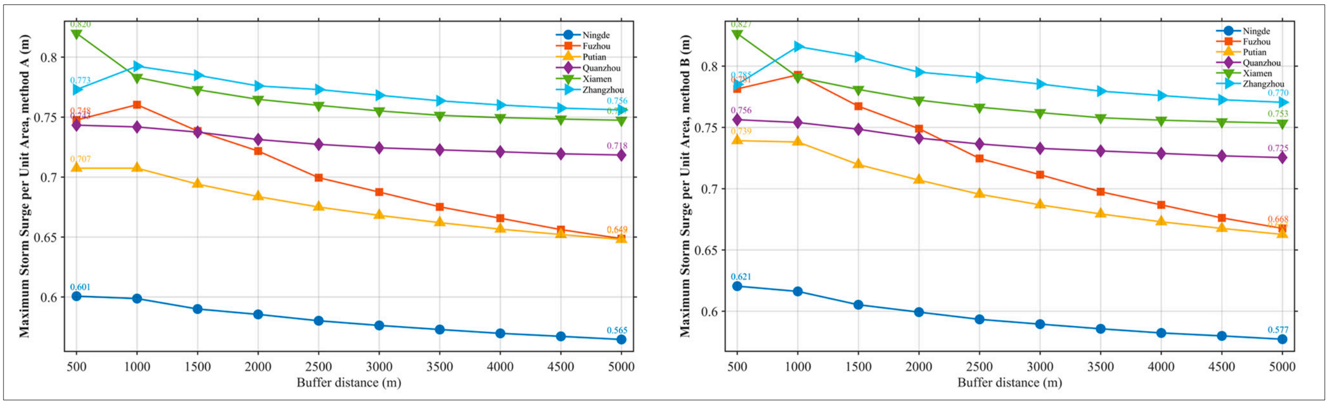

Figure 14. Line charts of maximum storm surge per unit area (1 m^2) vs. buffer distances (500–5000 m) in coastal waters near Ningde, Fuzhou, Putian, Quanzhou, Xiamen, and Zhangzhou. **Left**: Method A; **Right**: Method B.

This near-shore concentration reflects two complementary sets of causes. The first is physical mechanisms. Narrow coastal features such as shoals, tidal flats, estuarine channels and confined inlets promote geometric constriction and energy convergence, amplifying water levels via shallow-water nonlinearities, cross-shore convergence, and reflection; in very shallow zones, the coupling between wind stress and near-bed dynamics further enhances local sensitivity to meteorological forcing. The second is methodological and statistical factors. Area-weighted buffer statistics give greater weight to immediate nearshore elements in narrow bands, so narrow buffers emphasize node-scale maxima while wider buffers incorporate many lower-surge offshore elements that reduce the mean; additionally, finer nearshore mesh resolution increases the likelihood of resolving sharp local maxima, thereby amplifying the effect of node-based extraction.

Figure 14 also exposes clear spatial heterogeneity in Fujian's response to Typhoon Doksuri; different cities exhibit distinct cross-shore decay behaviors. For instance, Xiamen shows a relatively rapid decline in area-weighted peak between the 500 m and 1000 m bands (4.3%~4.5%), whereas Fuzhou exhibits a much larger cumulative decline across the 1000–5000 m range (14.7%~15.8%), indicating that Doksuri's nearshore amplification is more spatially concentrated in some locations than others. In contrast, cities such as Zhangzhou display much smaller buffer-scale declines and therefore a more diffuse surge footprint. These inter-city contrasts likely arise from the interplay of local geomorphology (presence, geometry and connectivity of shoals, tidal flats and channels), local hydrodynamic focusing, and the mesh resolution that governs how node-scale extremes are sampled.

Small percentage differences in surge estimates can have substantial implications for urban flood risk and infrastructure design, as minor variations in extreme water levels may translate into disproportionately large economic losses in coastal cities [9]. Therefore, high-resolution, physically consistent modeling frameworks—such as those resolving nearshore amplification and cyclone-induced extremes—are essential to provide reliable inputs for coastal adaptation and flood-protection planning [48].

3.3. Sea-Level Rise (SLR) Impacts on Storm Surge

Using the static SLR scenarios described in Section 2.4, we systematically assess the effect of SLR magnitude on extreme water levels. Figure 15 shows peak total water level and maximum storm surge at five representative tide stations under four SLR scenarios (0 m, +0.3 m, +0.5 m, +1.0 m). Figure 16 maps the spatial distributions of maximum storm surge and maximum total water level in the Xiamen nearshore under Method B for each

SLR case. Figure 17 depicts how area-normalized maximum surge at buffer scales responds to SLR for six coastal cities.

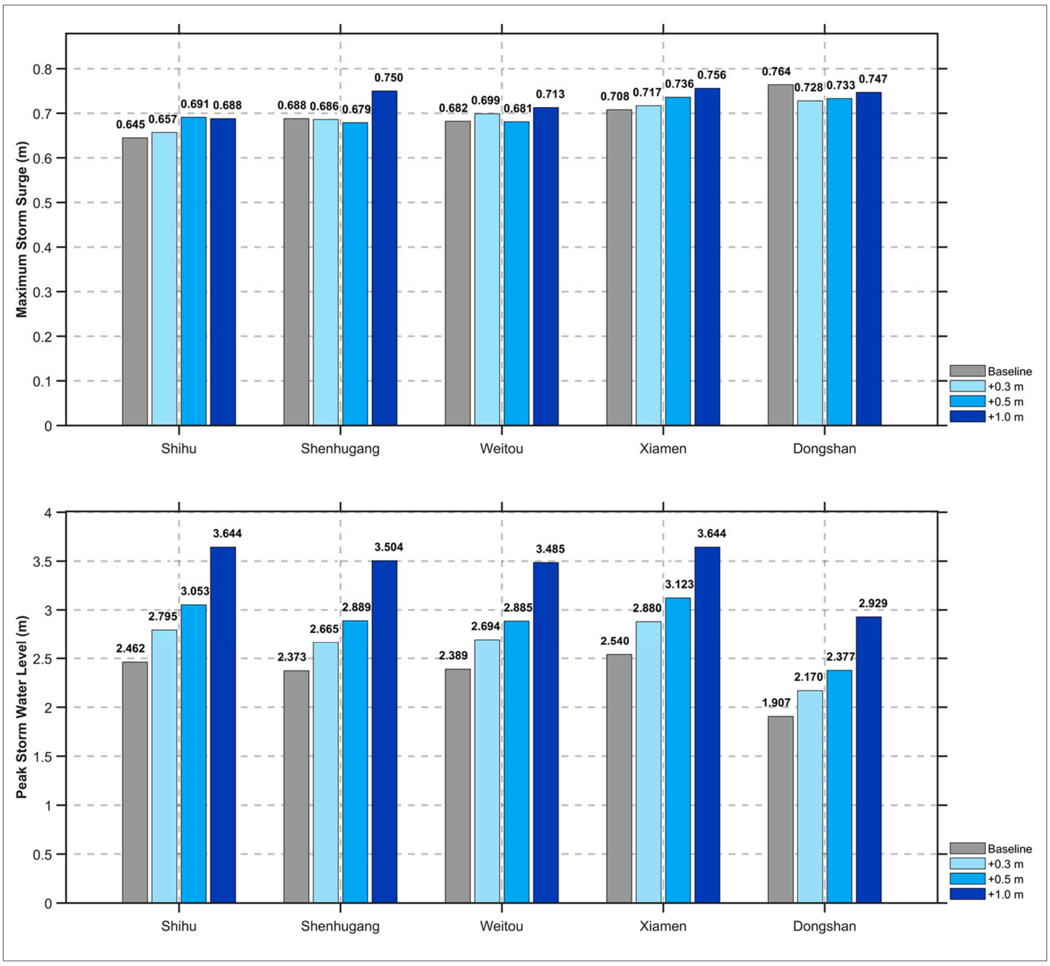

Figure 15. Bar charts of station-level maximum storm surge and maximum water level during storm surge under sea-level rise scenarios (0 m, 0.3 m, 0.5 m, 1 m). **Top**: maximum storm surge height (*Y*-axis). **Bottom**: maximum water level (*Y*-axis).

At the station scale, SLR produces a systematic uplift of peak total water levels. Under +0.3 m SLR total peaks increase by 0.263–0.340 m across stations; under +0.5 m, by 0.470–0.591 m; and under +1.0 m, by 1.022–1.182 m. The relationship between total peak increase and imposed SLR is approximately linear, consistent with multi-regional studies showing direct elevation of extreme water-level distributions under mean SLR [6,40]. Notably, under the +1.0 m scenario, some stations (e.g., Shihu) exhibit increases slightly larger than simple static superposition would predict, suggesting modest nonlinear amplification.

By contrast, the maximum storm surge component responds nonlinearly, and with marked spatial heterogeneity, to SLR. Changes in station maximum surge are much smaller than changes in total water level (typical magnitudes ±0.06 m) and vary by station; Shihu shows a fluctuating upward trend with SLR, Shenhugang decreases slightly under low-to-mid SLR and increases at +1.0 m, and Dongshan exhibits a monotonic decrease across SLR scenarios. These differing responses reflect complex modulation of surge by local bathymetry, tidal dynamics, and wind pressure coupling [24,40]. Such nonlinear and spatially heterogeneous responses to SLR are consistent with findings from other semi-enclosed systems, such as Laizhou Bay [49] and Chesapeake Bay [50], where local bathymetry and wetland migration were also found to modulate surge propagation and extreme water levels.

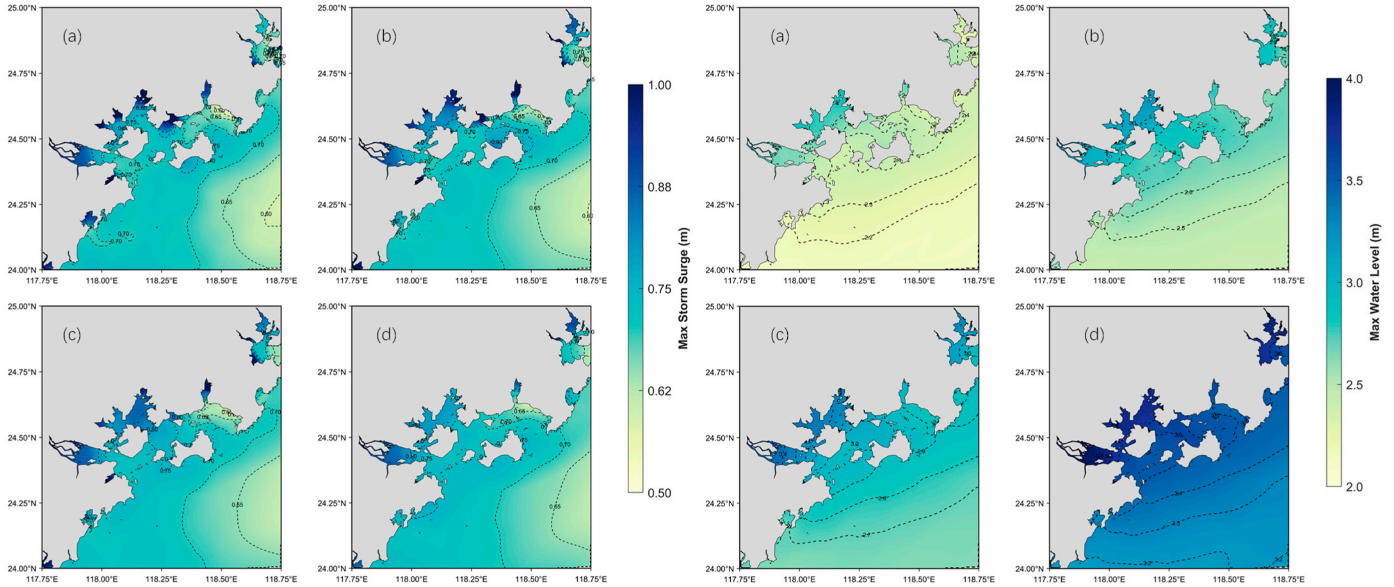

Figure 16. Maximum storm surge and water level in Xiamen coastal waters ((**a**–**d**) = SLR 0/0.3/0.5/1 m).

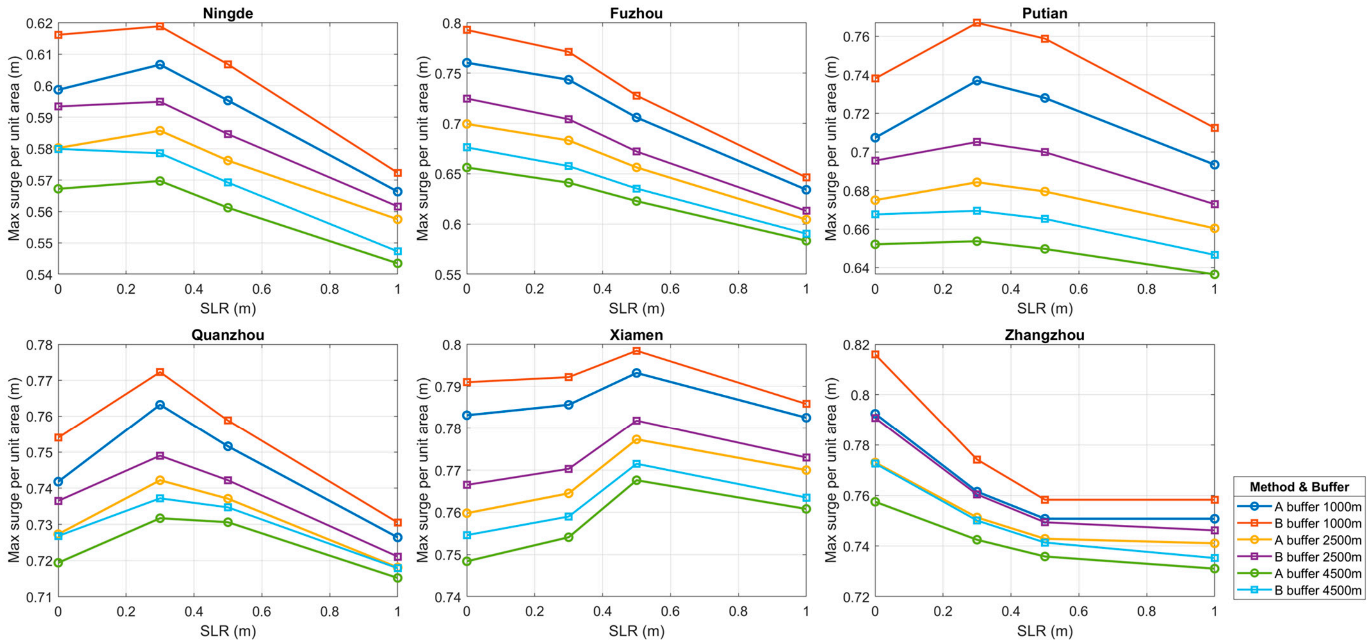

Figure 17. Area-normalized maximum storm surge response to sea-level rise (baseline–1.0 m) across buffer scales (1000 m, 2500 m, 4500 m) and extraction methods for six coastal cities in Fujian.

At the buffer scale, the response of the area-normalized maximum storm surge to sea-level rise (SLR) depends strongly on the spatial scale, the extreme-value extraction method, and local coastal geomorphology. As presented in Figure 17, the node-based extraction method (Method B) consistently yields higher area-normalized surge maxima than the cell-averaged method (Method A) for any given buffer width, owing to its ability to retain local peaks at narrow estuaries and shoals.

Under the different SLR scenarios (+0.3 m, +0.5 m, +1.0 m), the area-normalized surge exhibits two distinct spatial patterns.

The first pattern, observed in Fuzhou and Zhangzhou, is characterized by a nearly monotonic decrease with increasing SLR. For instance, at the 1000 m buffer using Method B, the area-normalized maximum surge in Fuzhou declines from 0.7929 m under the baseline to 0.6463 m under the +1.0 m SLR scenario; Zhangzhou shows a similar decreasing trend.

The second pattern, seen in Ningde, Quanzhou, Putian, and Xiamen, displays an initial increase under the low SLR scenario (+0.3 m) followed by a decrease under higher SLR increments. Taking Ningde as an example, at the 2500 m buffer and method A, the value rises from 0.5802 m in the baseline to 0.5857 m under +0.3 m SLR, then falls to 0.5575 m under the +1.0 m scenario.

These response trends remain consistent across all buffer widths. Moreover, the difference between the results obtained with Method A and Method B diminishes as the buffer width increase, indicating that regional averaging over a larger area smooths out local extremes.

The observed nonlinearity arises from a combination of physical and methodological mechanisms. In regions where the surge decreases monotonically (Pattern 1), the primary driver is likely the reduction in effective bottom friction as water depth increases, which allows surge-induced flows to disperse more efficiently and weakens shallow-water amplification. For instance, a decrease in the effective friction coefficient in estuarine regions such as the Minjiang River mouth could substantially reduce local surge peaks. Methodologically, the "dilution effect" also contributes as SLR expands the wetted area, the inclusion of more offshore elements with lower surge magnitudes statistically lowers the area-weighted mean.

The initial increase under low SLR (Pattern 2) can be attributed to a transient enhancement of local dynamics. Firstly, a limited water-level rise (+0.3 m) may temporarily strengthen topographic amplification in certain configurations, such as in semi-enclosed bays (e.g., Xiamen Bay) or funnel-shaped estuaries, where the existing geometry focuses surge energy more effectively under slightly increased depths. Secondly, SLR can modify the phasing between the astronomical tide and the storm surge component, potentially leading to a closer alignment of the surge peak with high tide under the +0.3 m scenario and thus a temporary synergistic increase. However, as SLR progresses to +0.5 m and +1.0 m, the continuing reduction in bottom friction and the growing importance of the statistical dilution effect eventually overwhelm these amplifying mechanisms, resulting in an overall decrease in area-normalized surge.

In summary, although extreme total water levels increase approximately linearly with SLR, the storm surge component itself exhibits a complex, spatially heterogeneous nonlinear response. This pattern reflects a dynamic balance among topographic focusing, frictional dissipation, and statistical averaging, underscoring the necessity of multi-scale and spatially explicit approaches for future SLR-informed coastal risk assessments.

3.4. Sensitivity Experiments

Using the parameter combinations designed in Section 2.7, we systematically evaluate the influence of bottom-friction parameterization and wind field intensity uncertainty on simulated outcomes. The bottom-friction sensitivity suite varies the bottom roughness parameter z_0 (0.00004–0.00012 m) and minimum drag coefficient $C_{d,\min}$ (0.00175–0.00525) across six cases; the wind intensity suite scales the anomalous wind component during peak periods by factors 0.8–1.2.

Tidal-only simulations indicate that station-scale tidal reconstruction is robust across these friction cases: Pearson correlation coefficients (r) at the five tide gauges remains in the 0.97–0.99 range and RMSE varies between 0.09 and 0.27 m (Figure 18), with only modest inter-case differences. This suggests limited sensitivity of bulk tidal amplitudes at the tested tide-gauge locations to the prescribed friction perturbations [21].

https://doi.org/10.3390/jmse14010005

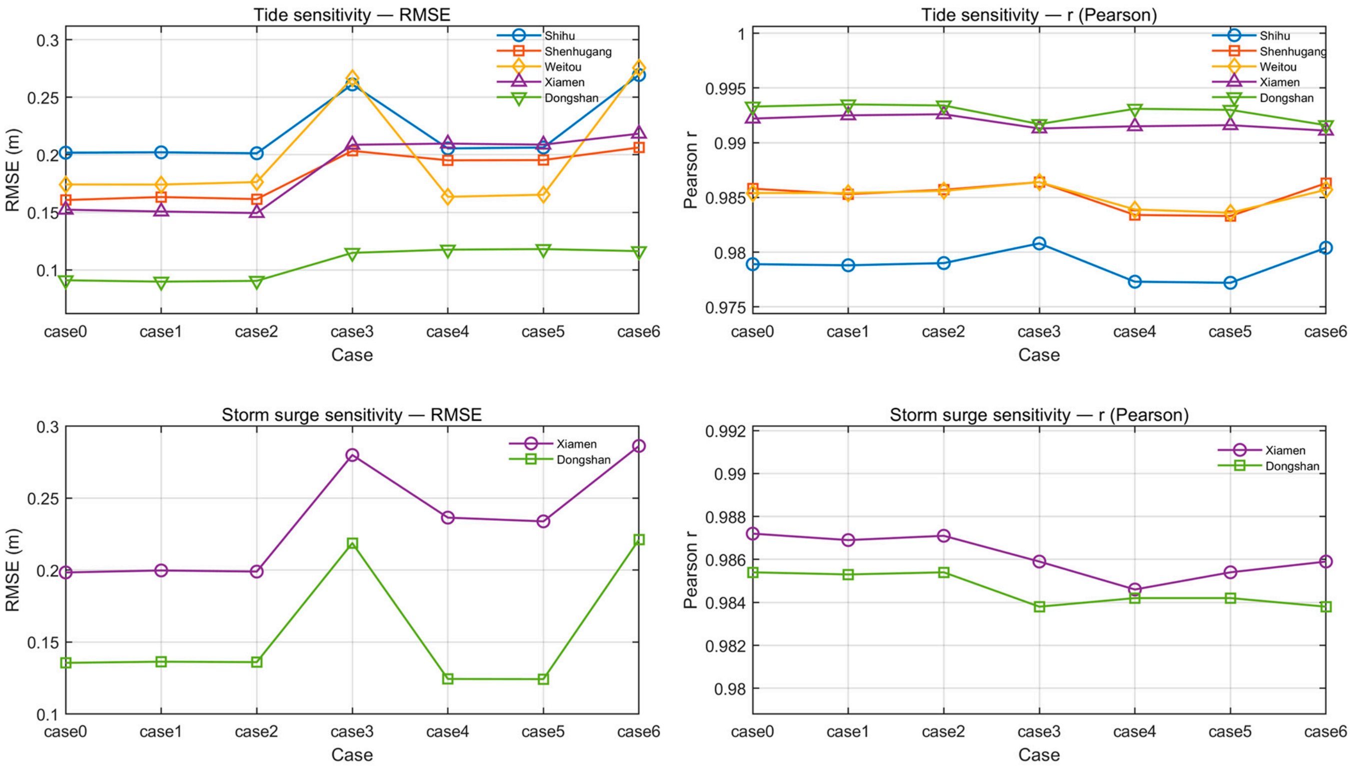

Figure 18. Line chart of bottom-friction sensitivity: RMSE and Pearson r across cases.

Validation of currents (Table 5; Appendix A, Table A2) reveals that the adjustments to bottom-friction parameters yield differentiated impacts across observation sites but do not lead to a consistent or substantial improvement in matching the observed velocity and direction. For instance, while Cases 3 and 6 improve speed RMSE at several stations (e.g., TSNM1 RMSE decreases from 0.0957 in Case 0 to 0.0885 in Case3, with Pearson r improving from 0.8896 to 0.9117), Cases 4 and 5 degrade speed accuracy at others (e.g., TSNM1 RMSE ≈ 0.105). Overall, the friction perturbations could not effectively enhance the model's skill in replicating the current patterns. Directional errors still remain, with RMSE ranging from 33.6° to 53.9° (Pearson r ≈ 0.47–0.89). These persistent discrepancies in both speed and direction suggest that the errors likely originate from other factors, such as inaccuracies in the bathymetric and topographic data, rather than from the parameterization of bottom friction alone.

Table 5. Selected validation metrics (speed RMSE and Pearson r) at four tidal-current stations for representative bottom-friction cases; full metrics for all cases are provided in Appendix A, Table A2.

Case	TSNM1 RMSE ($m{\cdot}s^{-1}$)	TSNM1 Pearson r	TSNM2 RMSE ($m{\cdot}s^{-1}$)	TSNM2 Pearson r	TSSM1 RMSE ($m{\cdot}s^{-1}$)	TSSM1 Pearson r	TSSM2 RMSE ($m{\cdot}s^{1}$)	TSSM2 Pearson r
case0	0.0957	0.8896	0.1248	0.926	0.1401	0.8306	0.1151	0.7897
case3	0.0885	0.9117	0.1134	0.9276	0.1099	0.8806	0.0898	0.8405
case6	0.0895	0.91	0.1131	0.9276	0.107	0.8852	0.088	0.8437
case4	0.105	0.8769	0.1304	0.9229	0.158	0.7946	0.1312	0.7554

Under storm conditions, the impact of bottom friction shows pronounced spatial heterogeneity. Xiamen achieves its best fit under the baseline and Case 2 parameters (Pearson r ≈ 0.987, RMSE ≈ 0.198 m), whereas Dongshan performs best when minimum drag coefficient $C_{d,\min}$ = 0.00525 (case4/case5; RMSE ≈ 0.124 m). Spatial maps of the surge difference (Case–Base) in Figure 19 further illustrate this complex response. The differences generally range between –0.3 m and +0.3 m. The color distribution in the figures clearly shows the spatial pattern; red areas indicate an increase in storm surge after perturbations to the bottom roughness parameter z_0 and minimum drag coefficient $C_{d,\min}$, while blue areas indicate a decrease. Specifically, Cases 3 and 6 induce increased surge (red) north of Taiwan Island but decreased surge (blue) in parts of the Taiwan Strait. These significant adjustments are predominantly concentrated in shallow and geometrically complex areas, whereas vast offshore and deeper regions (white) show minimal change. These inter-station contrasts reflect how friction modulates nearshore velocity structure, energy dissipation and tide–surge interactions; such spatially effects of bottom roughness parameter z_0 and minimum drag coefficient $C_{d,\min}$ on local tidal dynamics and extreme water levels have been documented in regional FVCOM studies [51].

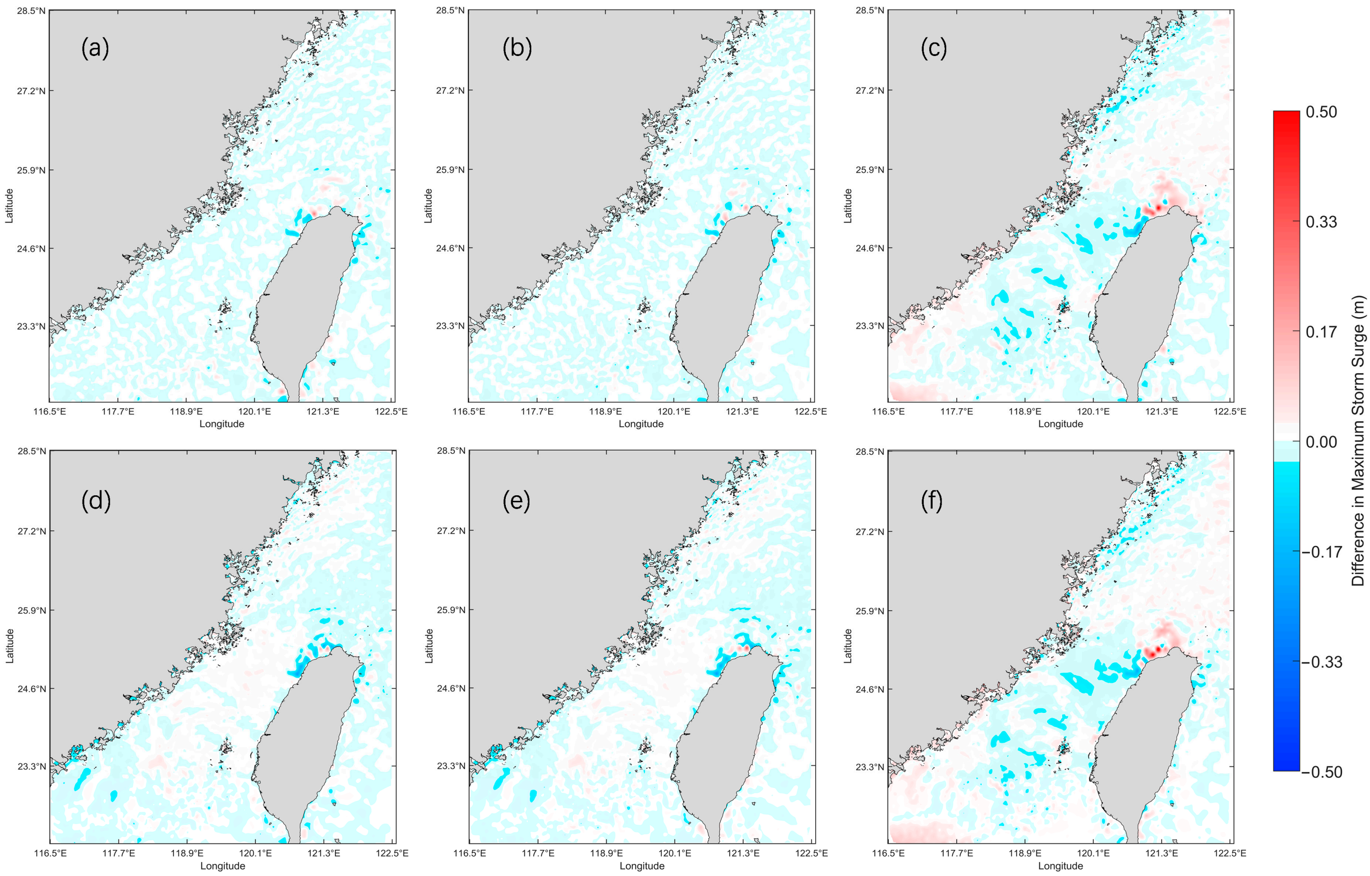

Figure 19. Spatial distribution maps of maximum storm surge difference (Case–Base) for friction sensitivity experiments ((**a**–**f**) = Case 1–Case 6).

Hourly statistics from the wind intensity sensitivity experiments show limited variation in station-level Pearson r, RMSE and bias at Xiamen and Dongshan across the ±20% wind-speed scenarios (Table 6), indicating a degree of robustness in time-series fit. However, spatial fields reveal a more complex, scale-dependent response (Figure 20); reducing the anomalous wind component to 0.8× typically decreases surge by ~0.10–0.20 m across broad nearshore areas, whereas amplifying winds to 1.2× can induce substantially larger, highly localized increases at sensitive features such as shoals and estuarine mouths. The response is markedly nonlinear and asymmetric—modest wind strengthening can trigger pronounced local amplification, while equivalent proportional wind weakening produces a comparatively muted suppression. This behavior reflects nonlinear coupling among wind stress, bathymetry, and tidal phase, and is consistent with previous work demonstrating that wind field errors and parameter choices can transfer nonlinearly into surge response and that local geomorphic and frictional settings modulate that transfer [12,45].

Consequently, when providing design surges for engineering applications, it is advisable to report both station-scale time-series metrics and spatial sensitivity ranges to capture this scale-dependent, nonlinear uncertainty.

Table 6. Statistical evaluation results of wind speed sensitivity experiments—effects of wind field intensity scaling factors (0.8–1.2) on storm surge at Xiamen and Dongshan stations.

Case	Scale	Station	Person r	Bias (m)	RMSE (m)
case0	1.0	Xiamen Dongshan	0.9872 0.9854	0.0795 −0.0009	0.1984 0.1356
case1	0.8	Xiamen Dongshan	0.9867 0.9853	0.0783 −0.0023	0.2009 0.1338
case2	0.9	Xiamen Dongshan	0.9868 0.9853	0.078 −0.0018	0.2002 0.135
case3	1.1	Xiamen Dongshan	0.9869 0.9857	0.0802 0.0007	0.2007 0.1363
case4	1.2	Xiamen Dongshan	0.9857 0.9858	0.0776 0.0018	0.2079 0.1374

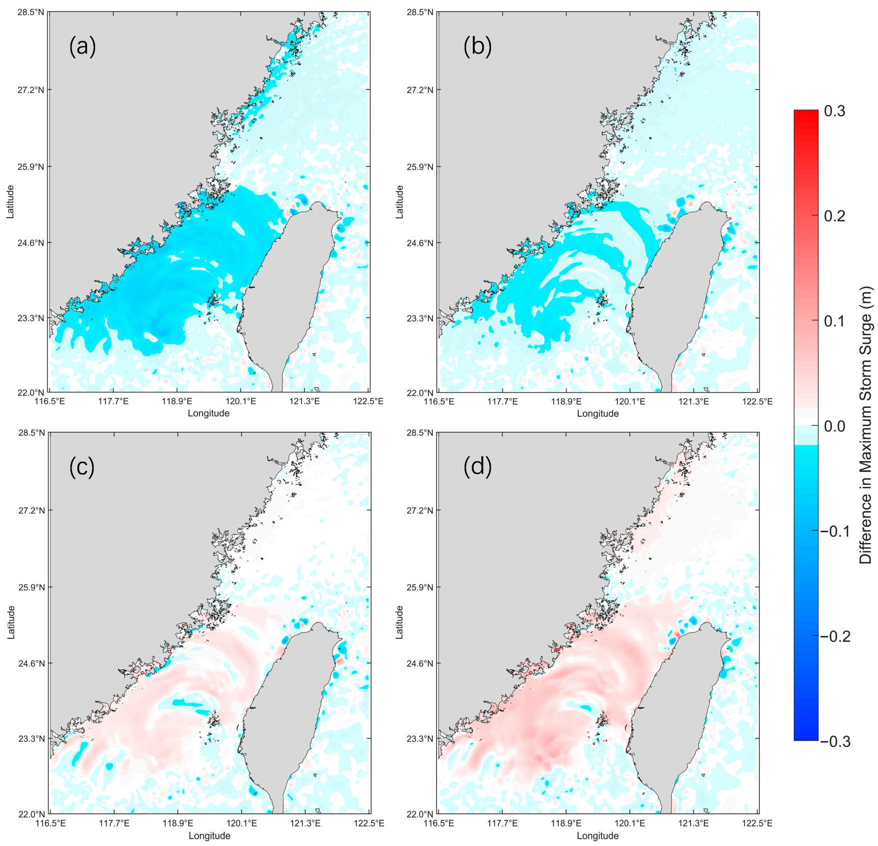

Figure 20. Spatial distribution of storm surge difference (Case–Base). Wind speed sensitivity Exp. ((**a**–**d**) = Case 1~Case 4).

In summary, the sensitivity experiments show that station-scale tidal reconstructions are broadly robust to the tested bottom-friction perturbations, whereas simulated surge peaks are highly sensitive in a spatially heterogeneous manner—with the largest friction-induced changes occurring in shallow, geometrically complex nearshore zones. Wind intensity uncertainty further modulates surge extremes through nonlinear and asymmetric mechanisms: modest wind strengthening can produce disproportionately large local amplifications at shoals and estuary mouths, while equivalent wind weakening yields comparatively muted reductions. Collectively, these results underscore the need to account explicitly for spatial sensitivity and nonlinear uncertainty when optimizing friction parameters and when reporting design surges for engineering applications (i.e., provide both station-scale fit metrics and spatial/ensemble sensitivity ranges to support uncertainty-aware risk assessment).

4. Discussion

4.1. Summary of Key Findings

Using a high-resolution FVCOM framework driven by a Holland–ERA5 hybrid wind field, this study successfully reproduced the storm surge events induced by Super Typhoon Doksuri (2023) in the coastal waters of Fujian. Model validation indicates strong performance—astronomical-tide Person r at five tide gauges ranges from 0.979 to 0.993, and hourly total water level time series at Xiamen and Dongshan achieve Pearson r = 0.987 and 0.985 with RMSE = 0.198 m and 0.136 m, respectively (Section 3.1). Surge maxima concentrate near 22:00–23:00 UTC on 27 July 2023. Pronounced local amplification was observed at nearshore shoals, bay entrances, and prominent headlands, where the maximum storm surge (purely meteorologically induced water level anomaly) exceeded 0.8 m locally (Figure 11). When combined with the astronomical tide, the resulting total water level reached heights above 2.8 m in these same sensitive areas (Figure 12).

Multi-scale buffer analysis revealed that the choice of extreme-value extraction method significantly influences estimated surge exposure; the node-based approach (Method B) systematically yielded local peaks that were 0.8% to 4.5% higher than those from the cell-averaged method (Method A), highlighting the critical role of method selection in applications requiring fidelity to local extremes, such as infrastructure design. Furthermore, surge magnitude was found to be strongly concentrated in the immediate nearshore.

Under static SLR scenarios, total peak water levels increased nearly linearly with SLR magnitude. In contrast, the storm surge component itself responded nonlinearly and showed strong spatial heterogeneity. This pattern suggests that elevated water depths may reduce bottom friction, thereby dampening shallow-water amplification, while the inclusion of more offshore areas in the averages statistically dilutes the normalized maxima.

Systematic sensitivity experiments further demonstrated that uncertainties in bottom friction and wind field intensity moderately yet distinctly affect surge simulations, with impacts that are spatially heterogeneous. Wind-speed perturbations, in particular, triggered strongly nonlinear and asymmetric surge responses, with localized amplification exceeding 0.15 m in sensitive shallow areas under a 1.2× wind scenario. These findings collectively yield important implications for coastal disaster mitigation and the development of uncertainty-aware risk assessments.

4.2. Physical Mechanisms Underlying Model Behavior

The strong spatial heterogeneity of the storm surge field arises from the combined action of three principal physical mechanisms. Firstly, the phase alignment of intense typhoon winds with the astronomical high tide produces marked peak amplification. When the storm's maximum wind sector coincides temporally with tidal high water, a phase-resonance effect substantially increases peak levels (observed enhancement in this study reaches ~35–40%; Figure 10), a mechanism that is particularly effective in the semidiurnal-tide regime of the Fujian coast.

Secondly, geometric confinement by nearshore bathymetry markedly modulates the water-level response. In narrow estuaries and recessed shorelines, flow is constrained by topography so that wind-driven water transport is concentrated, producing localized surge amplification. In classic complex-geometry areas such as the Minjiang estuary and Meizhou Bay, surge increases exceeding open-ocean values by ~20–30% (Figure 11) were observed, consistent with previous analyses of bathymetry–tide–wind coupling [8,24].

Thirdly, bottom friction controls energy dissipation with spatially varying effects. Sensitivity tests show that reducing the minimum drag coefficient $C_{d,\min}$ increases Pearson r by approximately 0.0015–0.0025 at some stations (e.g., Shihu, Shenhugang) but may also raise RMSE by ~0.05–0.06 m (Figure 18), reflecting a trade-off between improved phase reproduction and increased instantaneous error. This spatially heterogeneous response is physically consistent with bottom friction acting to modify nearshore velocity profiles and dissipative losses that influence local surge peaks [44].

Regarding wind forcing, blending the Holland parametric core with ERA5 reanalysis materially improves near-core intensity reproduction (Pearson r = 0.974), but uncertainties remain in eyewall asymmetry, post-landfall decay, and small-scale boundary-layer turbulence. These limitations contribute to systematic deviations of ~0.1–0.2 m at some extreme high-water instants (Section 3.1.4) and point to the need for further refinement of inner-core parameterizations and landfall boundary-layer representations [12].

4.3. Parameter Sensitivity and Spatially Heterogeneous Responses

Bottom-friction sensitivity experiments reveal distinct responses for tides and storm surge. Astronomical tides, governed mainly by boundary forcing, are largely insensitive to friction perturbations (station Pearson r remains 0.975–0.995 and RMSE changes < 0.10 m; Figure 18), consistent with theoretical expectations [21]. By contrast, surge peaks exhibit pronounced spatial heterogeneity. Evaluated by combined RMSE and Pearson r metrics, Xiamen attains optimal fit under baseline and Case 2 (moderate friction) settings ($r \approx 0.987$, RMSE ≈ 0.198 m), while Dongshan is better represented with an increased minimum friction (MIN = 0.00525; case4/5; RMSE ≈ 0.124 m) (Figure 18).

Mechanistically, these inter-site differences reflect coastal character; open, deeper segments preferentially transmit wind-generated energy, so lower friction promotes offshore-to-nearshore energy transfer; shallow shoals, estuaries and complex-geometry segments behave oppositely, where larger friction better represents bed roughness and dissipation, improving phase and local fit [R49]. Spatial maps (Figure 19) confirm that friction changes most strongly affect surge peaks in shallow and geometrically complex areas. Accordingly, increasing the spatial resolution of friction fields or applying data-assimilation-based friction inversion should improve local extreme-value reproduction.

Wind intensity perturbations produce strongly nonlinear and spatially dependent surge responses. Although station-level hourly statistics remain relatively stable across $\pm20\%$ wind-speed scaling (Table 6), spatial analyses reveal significant local differences (Figure 20); reducing peak wind to $0.8\times$ generally lowers maximum surge by ~0.10–0.20 m in most nearshore elements, whereas increasing wind to $1.2\times$ triggers pronounced local amplification in shoals and estuary mouths (typical increments ~0.15 m) concentrated in space. The response asymmetry arises from the nonlinear dependence of wind stress on wind speed (e.g., quadratic or higher-order) and the joint modulation by bathymetry and tidal phase—conditions under which modest wind strengthening more readily pushes the system into high-response regimes, whereas comparable weakening is partially buffered by dissipative processes [45,46]. Consequently, risk assessments and engineering designs should not rely on a single wind intensity scenario but instead incorporate ensembles or probabilistic scenarios to capture local vulnerability.

4.4. Implications for Engineering Practice and Risk Management

For short-term emergency warning and temporary protection (e.g., port operations, rapid shore reinforcement), we recommend small-scale buffers (500–1000 m) combined with node-based extreme extraction (Method B). This approach better detects local amplification—particularly in Fuzhou and Putian—identifying 3–4% higher peak risk relative to cell-averaged extraction (Method A) and thus supports targeted emergency decision-making [52].

For long-term planning and permanent infrastructure design (e.g., breakwater crest elevations, coastal-zone management), larger-scale statistics (2000–5000 m) combined with multi-scenario wind forcing are advised. Larger-area aggregation smooths local extremes, yielding more robust regional design values in line with conservative engineering practice [9]. At the same time, practitioners must account for the nonlinear transfer of wind intensity uncertainty to surge extremes (Section 3.4) by employing probabilistic or ensemble-based assessments [41].

Under sea-level rise, the results support adaptive, staged strategies. Although static SLR produces approximately linear increases in peak total water levels, the storm surge component responds nonlinearly and heterogeneously. We therefore advocate a "progressive-triggered" adaptation pathway: use the +0.3 m scenario to guide near-term measures, reserve capacity for +0.5–1.0 m in mid-to-long-term planning, and establish monitoring-triggered escalation procedures to activate upgrades if observed SLR exceeds expectations [40].

4.5. Study Limitations and Future Directions

Key limitations of the present study include the following: (1) the static SLR approach isolates direct elevation effects but does not consider potential climate-driven changes in tropical cyclone statistics (intensity, track, frequency) or long-term tidal evolution; (2) omission of a coupled wave model may underestimate wave-induced setup and radiation-stress contributions to total water level in shallow areas; and (3) the assumption of spatially uniform bottom-friction parameters departs from likely spatial heterogeneity, particularly in complex estuarine beds. Additionally, current-direction reproduction remains a shortcoming; although speed statistics are acceptable (Pearson r 0.79–0.93, RMSE 0.096–0.140 m/s), directional errors are comparatively large (Pearson r 0.50–0.88, RMSE 33.6–52.6°) [47]. These directional discrepancies primarily reflect mesh discretization of complex bathymetry, limited vertical resolution for shear-layer representation, and the uniform-friction assumption [10,32]. It is important to note that directional errors have a limited impact on the core conclusions regarding surge-peak water levels, given the model's strong performance in water-level metrics (astronomical tide Pearson $r = 0.979$–0.993; storm surge hourly Pearson $r > 0.98$) and the bounded sensitivity of peak levels to parameter uncertainty [41]. If future objectives include material transport, sediment dynamics, or ecological processes, resolving directional accuracy should be a priority. Moreover, (4) the study focuses on a single typhoon event (Doksuri), which, while providing an in-depth case analysis, limits the generalizability of findings across typhoons of varying intensities, tracks, and structures.

Future research will pursue coupled simulations that combine dynamic SLR scenarios with climate projections [53], the implementation of wave–storm surge coupling (e.g., FVCOM–SWAN) to improve shallow-water total-level estimates [54–56], the observationally based inversion of bottom-friction fields to develop spatially varying parameterizations, and the development of ensemble-based hybrid wind field construction methods to provide probabilistic forcing for risk assessments; comparative analyses across multiple typhoon cases to better understand the spectrum of surge responses, particularly for phenomena like left-side surges and variable tide-surge interactions, as documented in the region [57,58].

5. Conclusions

This study successfully reproduced the storm surge induced by Typhoon Doksuri (2023) in the complex coastal waters of Fujian, China, using a high-resolution FVCOM forced by a physically corrected Holland–ERA5 hybrid wind field. The model demonstrated high fidelity in simulating both astronomical tides (Pearson r = 0.979–0.993) and water level time series (Pearson r > 0.98) at key validation stations, with local surge maxima approaching 0.8 m and water level approaching 2.8 m.

The analysis revealed pronounced spatial heterogeneity in the surge response, identifying nearshore shoals, estuaries, and recessed shorelines as hotspots for strong local amplification. Systematic sensitivity experiments quantified that the effects of bottom friction are spatially dependent and that variations in wind field intensity modulate surge extremes through nonlinear mechanisms. Across the multi-scale buffer analysis, the node-based extraction (Method B) produces peak values that are 0.8% to 4.5% higher than those from the cell-averaged approach (Method A). Under static sea-level rise scenarios, the storm surge component exhibits a complex and spatially heterogeneous response—even decreasing in some nearshore zones. This behavior is likely due to the combined effects of elevated water depths reducing bottom friction and the incorporation of more offshore areas into spatial averages, which act to dampen shallow-water amplification mechanisms and dilute area-normalized maxima.

The integrated numerical framework and systematic analysis presented here provide a scientific foundation for storm surge risk assessment and disaster-reduction planning in the Fujian coastal region. For future work, it is recommended to develop a more comprehensive assessment framework that incorporates dynamic SLR projections, potential changes in tropical cyclone characteristics, wave–surge interactions, probabilistic methods, and adaptive planning strategies.

Author Contributions: Conceptualization, Z.X. and Y.L.; data curation, Z.X.; formal analysis, Z.X.; funding acquisition, Y.L.; investigation, Z.X.; methodology, Z.X.; project administration, Y.L.; resources, Y.L.; software, Z.X.; supervision, Y.L.; validation, Z.X. and Y.L.; visualization, Z.X.; writing—original draft, Z.X.; writing—review and editing, Z.X. and Y.L. All authors have read and agreed to the published version of the manuscript.

Funding: This research was funded by the Strategic Priority Research Program of the Chinese Academy of Sciences (grant number XDA23100504), and the Special Projects of the Central Government Guiding Local Science and Technology Development (grant number 2020L3005).

Data Availability Statement: The raw data supporting the conclusions of this article will be made available by the authors upon reasonable request. The ERA5 reanalysis data are publicly available from the Copernicus Climate Data Store at https://cds.climate.copernicus.eu/ (accessed on 18 April 2025). The typhoon best-track data were obtained from the China Meteorological Administration (CMA) Tropical Cyclone Data Center (https://typhoon.nmc.cn/web.html accessed on 7 January 2025). Access to these datasets is subject to the respective platforms' terms of use.

Acknowledgments: The authors acknowledge the data support from the European Centre for Medium-Range Weather Forecasts (ECMWF), the China Meteorological Administration (CMA), and the General Bathymetric Chart of the Oceans (GEBCO) project, in accordance with their respective data use policies. We also acknowledge the modeling capabilities provided by the Finite-Volume Coastal Ocean Model (FVCOM) community. Finally, we thank the editors and anonymous reviewers for their constructive feedback and efforts in enhancing this work, with their consent for this acknowledgment.

Conflicts of Interest: The authors declare no conflicts of interest.

Abbreviations

The following abbreviations are used in this manuscript:

TSNM1	Taiwan Strait Northern Mouth Station 1
n_elems	The number of elements
ECMWF	European Centre for Medium-Range Weather Forecasts
ERA5	ECMWF Atmospheric Reanalysis of the Global Climate (Fifth Generation)

Appendix A

Table A1. Full extraction results of maximum storm surge per unit area.

District	Buffer (m)	n_Elems	Band_Area (km^2)	Mean A (m)	Mean B (m)	Δ(B-A) (m)	Δ (%)
Ningde	500	931	274.5541	0.6007	0.6205	0.0198	3.30%
	1000	1583	484.0163	0.5987	0.6162	0.0175	2.92%
	1500	2283	723.7902	0.59	0.6053	0.0153	2.59%
	2000	2991	973.7683	0.5855	0.5993	0.0138	2.36%
	2500	3524	1171.566	0.5802	0.5934	0.0132	2.28%
Ningde	3000	4015	1368.541	0.5763	0.5895	0.0132	2.29%
	3500	4386	1523.562	0.5729	0.5857	0.0128	2.23%
	4000	4697	1661.933	0.5697	0.5823	0.0126	2.21%
	4500	4987	1799.67	0.5672	0.5799	0.0127	2.24%
	5000	5236	1921.982	0.5646	0.5772	0.0126	2.23%
Fuzhou	500	383	159.0355	0.7476	0.7814	0.0338	4.52%
	1000	729	315.0582	0.7603	0.7929	0.0326	4.29%
	1500	1194	531.0814	0.7384	0.7673	0.0289	3.91%
	2000	1462	663.3541	0.7217	0.749	0.0273	3.78%
	2500	1799	836.727	0.6995	0.7247	0.0252	3.60%
	3000	2029	960.7729	0.6875	0.7114	0.0239	3.48%
	3500	2263	1091.986	0.6752	0.6975	0.0223	3.30%
	4000	2472	1210.685	0.6657	0.6868	0.0211	3.17%
	4500	2667	1327.077	0.6562	0.6762	0.02	3.05%
	5000	2843	1434.301	0.6487	0.6676	0.0189	2.91%
Putian	500	259	122.0349	0.7074	0.7392	0.0318	4.50%
	1000	517	275.3598	0.7074	0.7381	0.0307	4.34%
	1500	814	425.1337	0.6941	0.7197	0.0256	3.69%
	2000	1039	551.4041	0.6837	0.707	0.0233	3.41%
	2500	1281	690.4442	0.675	0.6955	0.0205	3.04%
	3000	1483	810.8035	0.6681	0.6868	0.0187	2.80%
	3500	1670	925.9708	0.662	0.6794	0.0174	2.63%
	4000	1839	1036.669	0.6566	0.673	0.0164	2.50%
	4500	1992	1137.415	0.6521	0.6676	0.0155	2.38%
	5000	2132	1233.34	0.648	0.6627	0.0147	2.27%
Quanzhou	500	1036	149.2176	0.7433	0.7563	0.013	1.75%
	1000	1851	281.8289	0.7418	0.754	0.0122	1.64%
	1500	2507	421.6996	0.7375	0.7485	0.011	1.49%
	2000	3017	542.6033	0.7313	0.7413	0.01	1.37%
	2500	3412	640.4967	0.7273	0.7365	0.0092	1.26%
	3000	3793	744.8777	0.7244	0.7329	0.0085	1.17%
	3500	4084	826.8119	0.7227	0.7308	0.0081	1.12%
	4000	4363	908.7119	0.7211	0.7288	0.0077	1.07%
	4500	4614	978.7853	0.7194	0.7268	0.0074	1.03%
	5000	4842	1044.313	0.7184	0.7254	0.007	0.97%

Table A1. *Cont.*

District	Buffer (m)	n_Elems	Band_Area (km^2)	Mean A (m)	Mean B (m)	Δ(B-A) (m)	Δ (%)
Xiamen	500	1506	81.08486	0.8199	0.8266	0.0067	0.82%
	1000	2224	168.6431	0.7831	0.791	0.0079	1.01%
	1500	2773	230.4474	0.7729	0.781	0.0081	1.05%
	2000	3194	296.5451	0.7648	0.7723	0.0075	0.98%
	2500	3525	355.6445	0.7598	0.7665	0.0067	0.88%
	3000	3710	409.7326	0.7552	0.7621	0.0069	0.91%
	3500	3822	459.995	0.7515	0.7579	0.0064	0.85%
	4000	3947	527.176	0.7496	0.7559	0.0063	0.84%
	4500	4048	577.1405	0.7484	0.7546	0.0062	0.83%
	5000	4153	621.3297	0.7474	0.7535	0.0061	0.82%
Zhangzhou	500	115	60.10565	0.773	0.7851	0.0121	1.57%
	1000	219	177.7267	0.7924	0.816	0.0236	2.98%
	1500	309	256.7333	0.7849	0.8075	0.0226	2.88%
	2000	388	334.9987	0.776	0.7951	0.0191	2.46%
	2500	460	401.0536	0.773	0.7907	0.0177	2.29%
	3000	515	463.8878	0.7682	0.7854	0.0172	2.24%
	3500	576	540.4984	0.7636	0.7796	0.016	2.10%
	4000	610	598.2195	0.7601	0.776	0.0159	2.09%
	4500	642	646.6197	0.7575	0.7726	0.0151	1.99%
	5000	664	679.2224	0.756	0.7705	0.0145	1.92%

Table A2. Detailed validation statistics for the four tidal-current stations (TSNM1, TSNM2, TSSM1, TSSM2) across sensitivity cases (case0–case6). Units: speed RMSE (m·s^{-1}); direction RMSE (°).

Case	TSNM1 Speed RMSE (m·s^{-1})	TSNM1 Speed Pearson r	TSNM2 Speed RMSE (m·s^{-1})	TSNM2 Speed Pearson r	TSSM1 Speed RMSE (m·s^{-1})	TSSM1 Speed Pearson r	TSSM2 Speed RMSE (m·s^{-1})	TSSM2 Speed Pearson r
case0	0.0957	0.8896	0.1248	0.926	0.1401	0.8306	0.1151	0.7897
case1	0.0946	0.8917	0.1251	0.9263	0.1401	0.8302	0.1152	0.7893
case2	0.0954	0.8902	0.1249	0.9268	0.1402	0.8302	0.1151	0.7893
case3	0.0885	0.9117	0.1134	0.9276	0.1099	0.8806	0.0898	0.8405
case4	0.105	0.8769	0.1304	0.9229	0.158	0.7946	0.1312	0.7554
case5	0.1056	0.8759	0.1305	0.9231	0.1579	0.7952	0.1311	0.7569
case6	0.0895	0.91	0.1131	0.9276	0.107	0.8852	0.088	0.8437
Case	TSNM1 Dir RMSE (°)	TSNM1 Dir Pearson r	TSNM2 Dir RMSE (°)	TSNM2 Dir Pearson r	TSSM1 Dir RMSE (°)	TSSM1 Dir Pearson r	TSSM2 Dir RMSE (°)	TSSM2 Dir Pearson r
case0	38.62	0.5024	52.59	0.7123	33.61	0.8843	43.15	0.8423
case1	38.58	0.5046	52.66	0.7133	33.65	0.8837	43.29	0.8407
case2	38.72	0.5028	53.11	0.7106	33.65	0.8851	43.16	0.8411
case3	38.21	0.5431	50.28	0.7128	34.54	0.87	38.94	0.8558
case4	40.37	0.4749	53.71	0.7117	34.77	0.877	45.77	0.8302
case5	40.31	0.4759	53.88	0.7094	34.95	0.8761	46	0.8288
case6	38.02	0.5434	50.11	0.7114	36.55	0.8428	37.97	0.8584

References

1. Needham, H.F.; Keim, B.D.; Sathiaraj, D. A review of tropical cyclone-generated storm surges: Global data sources, observations, and impacts. *Rev. Geophys.* **2015**, *53*, 545–591. [CrossRef]
2. IPCC. *Climate Change 2021: The Physical Science Basis*; Contribution of Working Group I to the Sixth Assessment Report of the Intergovernmental Panel on Climate Change; Masson-Delmotte, V., Zhai, P., Pirani, A., Connors, S.L., Péan, C., Berger, S., Caud, N., Chen, Y., Goldfarb, L., Gomis, M.I., et al., Eds.; Cambridge University Press: Cambridge, UK, 2021.
3. Knutson, T.; Camargo, S.J.; Chan, J.C.L.; Emanuel, K.; Ho, C.-H.; Kossin, J.; Mohapatra, M.; Satoh, M.; Sugi, M.; Walsh, K.; et al. Tropical cyclones and climate change assessment: Part II: Projected response to anthropogenic warming. *Bull. Am. Meteorol. Soc.* **2020**, *101*, E303–E322. [CrossRef]
4. Mei, W.; Xie, S.-P. Intensification of landfalling typhoons over the Northwest Pacific since the late 1970s. *Nat. Geosci.* **2016**, *9*, 753–757. [CrossRef]
5. Kossin, J.P.; Emanuel, K.A.; Vecchi, G.A. The poleward migration of the location of tropical cyclone maximum intensity. *Nature* **2014**, *509*, 349–352. [CrossRef]

6. Vousdoukas, M.I.; Mentaschi, L.; Voukouvalas, E.; Verlaan, M.; Jevrejeva, S.; Jackson, L.P.; Feyen, L. Global probabilistic projections of extreme sea levels show intensification of coastal flood hazard. *Nat. Commun.* **2018**, *9*, 2360. [CrossRef]
7. Kirezci, E.; Young, I.R.; Ranasinghe, R.; Muis, S.; Nicholls, R.J.; Lincke, D.; Hinkel, J. Projections of global-scale extreme sea levels and resulting episodic coastal flooding over the 21st Century. *Sci. Rep.* **2020**, *10*, 11629. [CrossRef]
8. Guo, W.Y.; Yao, D.; Chen, Z.; Ding, P.X.; Ge, J.Z. Assessment of future flood risk induced by sea level rise and tropical cyclones under global warming in the Xiamen Bay, Fujian, China. *Front. Mar. Sci.* **2023**, *10*, 1103279. [CrossRef]
9. Hallegatte, S.; Green, C.; Nicholls, R.J.; Corfee-Morlot, J. Future flood losses in major coastal cities. *Nat. Clim. Change* **2013**, *3*, 802–806. [CrossRef]
10. Chen, C.; Liu, H.; Beardsley, R.C. An unstructured grid, finite-volume, three-dimensional, primitive equations ocean model: Application to coastal ocean and estuaries. *J. Atmos. Ocean. Technol.* **2003**, *20*, 159–186. [CrossRef]
11. Copernicus Climate Change Service (C3S). ERA5 Hourly Data on Single Levels from 1940 to Present. Copernicus Climate Change Service (C3S) Climate Data Store (CDS). 2023. Available online: https://cds.climate.copernicus.eu/datasets/reanalysis-era5-single-levels?tab=overview (accessed on 18 April 2025).
12. Xiong, J.; Yu, F.J.; Fu, C.F.; Dong, J.X.; Liu, Q.X. Evaluation of the ERA5 wind field in typhoon storm surge simulations. *Appl. Ocean Res.* **2022**, *118*, 103000. [CrossRef]
13. Holland, G.J. An analytic model of the wind and pressure profiles in hurricanes. *Mon. Weather Rev.* **1980**, *108*, 1452–1464. [CrossRef]
14. Liu, F.; Sasaki, J. Hybrid methods combining atmospheric reanalysis data and a parametric typhoon model to hindcast storm surges in Tokyo Bay. *Sci. Rep.* **2019**, *9*, 12222. [CrossRef]
15. Shao, Z.X.; Liang, B.C.; Li, H.J.; Wu, G.X.; Wu, Z.H. Blended wind fields for wave modeling of tropical cyclones in the South China Sea and East China Sea. *Appl. Ocean Res.* **2018**, *71*, 20–33. [CrossRef]
16. Jiao, L.; Liu, C.; Jiang, D.; Zhang, X.; Lv, X. Storm surge numerical simulation of Typhoon "Mangkhut" with adjoint data assimilation. *J. Mar. Sci. Eng.* **2025**, *13*, 1992. [CrossRef]
17. Chen, F.; Ding, K.; Sun, Z. Effect of nonlinear factors on typhoon-induced storm surges. *J. Mar. Sci. Eng.* **2025**, *13*, 5. [CrossRef]
18. Zhang, X.; Zuo, C.; Wang, Z.; Tao, C.; Han, Y.; Zuo, J. Typhoon storm surge simulation study based on reconstructed ERA5 wind fields—A case study of Typhoon "Muifa", the 12th Typhoon of 2022. *J. Mar. Sci. Eng.* **2024**, *12*, 2099. [CrossRef]
19. Zhang, B.; Li, X.; Wang, L.; Gao, Y. Numerical Simulation of Typhoon Waves in an Offshore Wind Farm Area of the South China Sea. *J. Mar. Sci. Eng.* **2025**, *13*, 451. [CrossRef]
20. Suh, S.W.; Lee, H.Y.; Kim, H.J.; Fleming, J.G. An efficient early warning system for typhoon storm surge based on time-varying advisories by coupled ADCIRC and SWAN. *Ocean Dyn.* **2015**, *65*, 617–646. [CrossRef]
21. Qian, S.; Du, Y.; Wei, Z.; Zhang, J.; Cheng, J.; Wang, D.; Wang, Y.P. Effects of spatial bottom friction parameterization scheme on the tidal dynamics in the macrotidal East China Seas. *Front. Mar. Sci.* **2023**, *10*, 1085118. [CrossRef]
22. Zhang, Y.; Ji, Q.; Xie, M.; Wu, Y.; Tian, Y. Wave–tide interaction by Typhoon Ampil on wave and storm surge in the Changjiang River Estuary and its adjacent coastal areas. *J. Mar. Sci. Eng.* **2023**, *11*, 1984. [CrossRef]
23. Peng, Z.-Y.; Wang, P. Surface Wave Effects on Storm Surge: A Case Study of Typhoon Doksuri (2023). *J. Mar. Sci. Eng.* **2025**, *13*, 478. [CrossRef]
24. De Dominicis, M.; Wolf, J.; Jevrejeva, S.; Zheng, P.; Hu, Z. Future interactions between sea level rise, tides, and storm surges in the world's largest urban area. *Geophys. Res. Lett.* **2020**, *47*, e2020GL087002. [CrossRef]
25. Talke, S.A.; Familkhalili, R.; Jay, D.A. The influence of channel deepening on tides, river discharge effects, and storm surge. *J. Geophys. Res. Oceans* **2021**, *126*, e2020JC016328. [CrossRef]
26. GEBCO Bathymetric Compilation Group. *The GEBCO_2023 Grid—A Continuous Terrain Model of the Global Oceans and Land (GEBCO_2023)*; NERC EDS British Oceanographic Data Centre NOC: Liverpool, UK, 2023. [CrossRef]
27. *Global Self-Consistent, Hierarchical, High-Resolution Geography Database (GSHHG)*, Version 2.3.7; University of Hawaii: Honolulu, HI, USA, 2017.
28. Zhongke Tuxin (Suzhou) Technology Co., Ltd. *LocaSpace Viewer 4 [CP/OL]*, Version 4.5.2. 2025. Available online: http://www.tuxingis.com/locaspace.html (accessed on 18 April 2025).
29. Li, M.; Zheng, J. Introduction to Chinatide Software for Tide Prediction in China Seas. *J. Waterw. Harb.* **2007**, *28*, 65–68.
30. Fan, C. Latest Advances of Global Ocean Tide Models and Their Accuracy Comparisons in Coastal Areas of China. *J. Geod. Geodyn.* **2019**, *39*, 476–481.
31. Mellor, G.L.; Yamada, T. Development of a turbulence closure model for geophysical fluid problems. *Rev. Geophys.* **1982**, *20*, 851–875. [CrossRef]
32. Dukhovskoy, D.S.; Morey, S.L. Simulation of the Hurricane Dennis storm surge and considerations for vertical resolution. *Nat. Hazards* **2011**, *58*, 511–540. [CrossRef]
33. Shchepetkin, A.F.; McWilliams, J.C. The regional oceanic modeling system (ROMS): A split-explicit, free-surface, topography-following-coordinate oceanic model. *Ocean Model.* **2005**, *9*, 347–404. [CrossRef]

34. Zhang, J.C.; Lu, X.Q.; Wang, P.; Wang, Y.P. Study on linear and nonlinear bottom friction parameterizations for regional tidal models using data assimilation. *Cont. Shelf Res.* **2011**, *31*, 555–573. [CrossRef]
35. Hersbach, H.; Bell, B.; Berrisford, P.; Hirahara, S.; Horanyi, A.; Munoz-Sabater, J.; Nicolas, J.; Peubey, C.; Radu, R.; Schepers, D.; et al. The ERA5 global reanalysis. *Q. J. R. Meteorol. Soc.* **2020**, *146*, 1999–2049. [CrossRef]
36. Graham, H.E.; Hudson, G.N. *Surface Winds Near the Center of Hurricanes (and Other Cyclones)*; National Hurricane Research Project Report; U.S. Weather Bureau: Washington, DC, USA, 1960; Volume 39, pp. 1–200.
37. Vickery, P.J.; Wadhera, D. Statistical models of Holland pressure profile parameter and radius to maximum winds of hurricanes from flight-level pressure and HWind data. *J. Appl. Meteorol. Climatol.* **2008**, *47*, 1033–1048. [CrossRef]
38. Iwamoto, T.; Takagawa, T.; Shibayama, T.; Esteban, M.; Mäll, M. A proposal of a semi-empirical method for modifying the atmospheric pressure and wind fields of tropical cyclones. *Coast. Eng. J.* **2023**, *65*, 418–432. [CrossRef]
39. Kaplan, J.; DeMaria, M. A simple empirical model for predicting the decay of tropical cyclone winds after landfall. *J. Appl. Meteorol. Climatol.* **1995**, *34*, 2499–2512. [CrossRef]
40. Kopp, R.E.; Horton, R.M.; Little, C.M.; Mitrovica, J.X.; Oppenheimer, M.; Rasmussen, D.J.; Strauss, B.H.; Tebaldi, C. Probabilistic 21st and 22nd century sea-level projections at a global network of tide-gauge sites. *Earth's Future* **2014**, *2*, 383–406. [CrossRef]
41. Lin, N.; Emanuel, K.; Oppenheimer, M.; Vanmarcke, E. Physically based assessment of hurricane surge threat under climate change. *Nat. Clim. Change* **2012**, *2*, 462–467. [CrossRef]
42. Luettich, R.A., Jr.; Westerink, J.J.; Scheffner, N.W. *ADCIRC: An Advanced Three-Dimensional Circulation Model for Shelves, Coasts, and Estuaries*; Theory and Methodology of ADCIRC-2DDI and ADCIRC-3DL; Technical Report No. CERCTRDRP926; Defense Technical Information Center: Richmond, VA, USA, 1992.
43. Wang, F.; Liu, X.Z.; Li, Y.; Yu, H.; Wen, M.Z.; Hu, Y.Z. Risk assessment of coastal flooding disaster by storm surge based on Elevation-Area method and hydrodynamic models: Taking Bohai Bay as an example. *China Geol.* **2024**, *7*, 494–504. [CrossRef]
44. Wang, D.; Zhang, J.; Wang, Y.P. Estimation of bottom friction coefficient in multi-constituent tidal models using the adjoint method: Temporal variations and spatial distributions. *J. Geophys. Res. Oceans* **2021**, *126*, e2020JC016949. [CrossRef]
45. Chu, D.D.; Zhang, J.C.; Wu, Y.S.; Jiao, X.H.; Qian, S.H. Sensitivities of modelling storm surge to bottom friction, wind drag coefficient, and meteorological product in the East China Sea. *Estuar. Coast. Shelf Sci.* **2019**, *231*, 106460. [CrossRef]
46. Large, W.G.; Pond, S. Open ocean momentum flux measurements in moderate to strong winds. *J. Phys. Oceanogr.* **1981**, *11*, 324–336. [CrossRef]
47. Liu, W.; Zheng, Q.; Wang, Z.; Zuo, J. Comparative Analysis of Hydrodynamic Characteristics off Shandong Under the Influence of Two Types of Storm Surges. *J. Mar. Sci. Eng.* **2025**, *13*, 1054. [CrossRef]
48. Muis, S.; Verlaan, M.; Winsemius, H.; Aerts, J.; Ward, P.J. A global reanalysis of storm surges and extreme sea levels. *Nat. Commun.* **2016**, *7*, 11969. [CrossRef]
49. Shi, H.; Zhao, S.; Zhu, R.; Sun, L.; Wang, H.; Wang, Q.; Zhan, C. Risk assessment of storm surge disasters in a semi-enclosed bay under the influence of cold waves: A case study of Laizhou Bay, China. *J. Mar. Sci. Eng.* **2025**, *13*, 1434. [CrossRef]
50. Bigalbal, A.; Rezaie, A.M.; Garzon, J.L.; Ferreira, C.M. Potential impacts of sea level rise and coarse scale marsh migration on storm surge hydrodynamics and waves on coastal protected areas in the Chesapeake Bay. *J. Mar. Sci. Eng.* **2018**, *6*, 86. [CrossRef]
51. Wang, X.; Verlaan, M.; Veenstra, J.; Lin, H.X. Data-assimilation-based parameter estimation of bathymetry and bottom friction coefficient to improve coastal accuracy in a global tide model. *Ocean Sci.* **2022**, *18*, 881–904. [CrossRef]
52. Coles, S.; Bawa, J.; Trenner, L.; Dorazio, R.M. *An Introduction to Statistical Modeling of Extreme Values*; Springer: London, UK, 2001.
53. Jebbad, R.; Sierra, J.P.; Gironella, X.; Mösso, C.; González-Marco, D.; Lionello, P. Uncertainty in the Assessment of Wave Overtopping in Mediterranean Moroccan Ports Associated with Climate Change. *J. Mar. Sci. Eng.* **2025**, *13*, 2021. [CrossRef]
54. Chen, T.Q.; Zhang, Q.H.; Wu, Y.S.; Ji, C.; Yang, J.S.; Liu, G.W. Development of a wave-current model through coupling of FVCOM and SWAN. *Ocean Eng.* **2018**, *164*, 443–454. [CrossRef]
55. Yang, Z.; Shao, W.; Ding, Y.; Shi, J.; Ji, Q. Wave simulation by the SWAN model and FVCOM considering the sea-water level around the Zhoushan Islands. *J. Mar. Sci. Eng.* **2020**, *8*, 783. [CrossRef]
56. Chi, Y.; Rong, Z. Assessment of extreme storm surges over the Changjiang River Estuary from a wave-current coupled model. *J. Mar. Sci. Eng.* **2021**, *9*, 1222. [CrossRef]
57. Wan, W.Q.; Feng, X.R.; Yin, B.S.; Liu, Q.R. Explanations for the positive storm surges on the left side of landfall typhoons in China. *Front. Mar. Sci.* **2024**, *11*, 1401110. [CrossRef]
58. Chen, Y.; Miao, Y.T.; Xie, P.W.; Zhang, Y.H.; Li, Y.N. Tide-surge interactions in Northern South China Sea: A comparative study of Barijat and Mangkhut (2018). *Front. Mar. Sci.* **2024**, *11*, 1423294. [CrossRef]

Disclaimer/Publisher's Note: The statements, opinions and data contained in all publications are solely those of the individual author(s) and contributor(s) and not of MDPI and/or the editor(s). MDPI and/or the editor(s) disclaim responsibility for any injury to people or property resulting from any ideas, methods, instructions or products referred to in the content.